

Article

Not peer-reviewed version

---

# The Gateway to Parallel Universe & Connected Physics

---

[Deep Bhattacharjee](#)<sup>\*</sup>, [Onwuka Frederick](#)<sup>\*</sup>, [Riddhima Sadhu](#), [Susmita Bhattacharjee](#)<sup>\*</sup>,  
Shounak Bhattacharya, [Soumendra Nath Thakur](#), Priyanka Samal<sup>\*</sup>, [Pallab Nandi](#)<sup>\*</sup>, [Tarun Bhattacharjee](#),  
Sanjeevan Singha Roy<sup>\*</sup>, Ranjan Ghora, Ranjan Patra

Posted Date: 11 March 2026

doi: 10.20944/preprints202104.0350.v2

Keywords: parallel universe; cosmic microwave background radiation; quantum entanglement






Preprints.org is a free multidisciplinary platform providing preprint service that is dedicated to making early versions of research outputs permanently available and citable. Preprints posted at Preprints.org appear in Web of Science, Crossref, Google Scholar, Scilit, Europe PMC.

Copyright: This open access article is published under a [Creative Commons CC BY 4.0 license](#), which permit the free download, distribution, and reuse, provided that the author and preprint are cited in any reuse.

Disclaimer/Publisher's Note: The statements, opinions, and data contained in all publications are solely those of the individual author(s) and contributor(s) and not of MDPI and/or the editor(s). MDPI and/or the editor(s) disclaim responsibility for any injury to people or property resulting from any ideas, methods, instructions, or products referred to in the content.

Article

# The Gateway to Parallel Universe & Connected Physics

Deep Bhattacharjee <sup>1,\*</sup> , Onwuka Frederick <sup>2,\*</sup>, Riddhima Sadhu <sup>3</sup>, Susmita Bhattacharjee <sup>4,\*</sup>, Shounak Bhattacharya <sup>5</sup>, Soumendra Nath Thakur <sup>6</sup>, Priyanka Samal <sup>7,\*</sup> , Pallab Nandi <sup>8,\*</sup>, Tarun Bhattacharjee <sup>9</sup>, Sanjeevan Singha Roy <sup>10,\*</sup> , Ranjan Ghora <sup>11</sup> and Ranjan Patra <sup>12</sup>

<sup>1</sup> Electro-Gravitational Space Propulsion Laboratory (EGSPL), India

<sup>2</sup> Ekiti State University, Ado-Ekiti, Nigeria

<sup>3</sup> Birla Institute of Technology (BIT) Mesra, Ranchi, India

<sup>4</sup> Researcher in Theoretical Physics, Kolkata, India

<sup>5</sup> Asian College of Teachers, Kolkata, India

<sup>6</sup> Tagore's Electronic Lab, Kolkata, India

<sup>7</sup> Independent Researcher, India

<sup>8</sup> Former Student of Indian Institute of Science Education and Research (IISER), Kolkata, India

<sup>9</sup> Independent Researcher, India

<sup>10</sup> Birla Institute of Technology (BIT) Mesra, India

<sup>11</sup> Independent Researcher, Uttar Pradesh, India

<sup>12</sup> Independent Researcher, Odisha, India

\* Correspondence: itsdeep@live.com (D.B.); frederickonwuka16@gmail.com (O.F.); itsvividcosmos@gmail.com (S.B.); priyankasamal9437@gmail.com (P.S.); pallabnandi995@gmail.com (P.N.); sanjeevan9905@gmail.com (S.S.R.)

## Abstract

The Cosmic Microwave Background Radiation (CMBR) harbours a cold spot in the southern celestial hemisphere — the so-called *Eridanus Supervoid* — whose anomalous temperature depression of  $\sim 70 \mu\text{K}$  and spatial extent of roughly 300 Mpc at redshift  $z \approx 1$  resist explanation within a purely Gaussian, single-universe framework. In this work we develop a self-consistent theoretical programme that interprets this cold spot as a relic imprint of a *conjugate parallel universe* that shared a common inflationary epoch with our own before separating under a spontaneous symmetry-breaking transition. Our formalism is built upon three interlocking pillars. First, we introduce a *two-dimensional imaginary time topology* in which the temporal coordinate is promoted from a one-dimensional real line  $\mathbb{R}^1$  to a pair of complex curves  $C^1$  and  $C^2$  embedded in the  $\mathbb{R}^3$  manifold. The two curves carry opposite orientation angles of  $\pm 2\pi i$ , yielding an affine parameter of  $\pi$  for the coupled system. Second, we derive the *entanglement entropy* of the universe pair by treating each universe as a quantum object with an imaginary-time Ket vector; the Von Neumann entropy of the resulting density matrix links macroscopic cosmological observables to quantum information-theoretic quantities. Third, we embed the birth and separation of the twin universes within Perelman's Ricci-flow surgery framework, identifying the blow-up of a curvature singularity as the topological mechanism responsible for the universal split. In addition, the paper addresses the holomorphic structure of pre- and post-Big Bang time, the non-Gaussian cosmic-texture signatures of the cold spot, a simulation-based glitch matrix, Jacobi-field analysis of the junction conditions, and the phenomenological implications for the Mandela effect, *déjà vu*, and related confabulation phenomena. The paper concludes with a probabilistic treatment of conjugate-universe counting within a landscape of  $10^{500}$  vacua and a comprehensive statistical analysis supporting the twin-universe conjecture.

**Keywords:** parallel universe; cosmic microwave background radiation; quantum entanglement

**PACS:** 98.80.Cq (Particle-physics and field-theory models of the early Universe); 98.80.Es (Observational cosmology); 04.50.Kd (Modified theories of gravity); 03.65.Ud (Entanglement and quantum nonlocality); 05.70.Ln (Nonequilibrium and irreversible thermodynamics)

**MSC: MSC2020 Primary:** 83F05 (Relativistic cosmology); **MSC2020 Secondary:** 83E30 (String and superstring theories); 53C44 (Geometric flows); 81P40 (Quantum coherence and entanglement); 37N20 (Dynamical systems in other branches of physics)

## 1. Introduction and Observational Motivation

### 1.1. The Cosmic Microwave Background Radiation

The Cosmic Microwave Background Radiation (CMBR) is the relic thermal radiation field that permeates the universe, originating approximately 380,000 years after the Big Bang when the primordial plasma cooled sufficiently for hydrogen atoms to form — an epoch known as *recombination*. At that moment, photons decoupled from matter and streamed freely through the nascent universe, carrying with them a snapshot of the primordial density field. Today the CMBR manifests as an extraordinarily uniform bath of microwave photons with a blackbody temperature of

$$T_{\text{CMB}} = 2.7255 \pm 0.0006 \text{ K}, \quad (1)$$

as established by the FIRAS instrument aboard the COBE satellite (Fixsen et al. 1996). Despite this isotropy at the level of one part in  $10^5$ , the CMBR encodes a rich structure of temperature anisotropies that provides the primary observational window into early-universe cosmology.

The power spectrum of temperature fluctuations is conventionally decomposed into spherical harmonics:

$$T(\theta, \varphi) = \sum_{\ell=0}^{\infty} \sum_{m=-\ell}^{\ell} a_{\ell m} Y_{\ell m}(\theta, \varphi), \quad (2)$$

where  $a_{\ell m}$  are the multipole coefficients and  $Y_{\ell m}$  are the standard spherical harmonics. The angular power spectrum is

$$C_{\ell} \equiv \langle |a_{\ell m}|^2 \rangle = \frac{1}{2\ell + 1} \sum_{m=-\ell}^{\ell} |a_{\ell m}|^2. \quad (3)$$

Figure ?? illustrates the characteristic Sachs–Wolfe plateau at low  $\ell$ , the acoustic peaks, and the Silk damping tail as measured by WMAP (Hinshaw et al. 2013) and the Planck satellite (Planck Collaboration 2020). The  $\Lambda$ CDM model fits the data exquisitely across a range spanning four orders of magnitude in multipole moment.

### 1.2. Anomalies in the CMBR

Notwithstanding the success of the concordance cosmology, several large-scale anomalies persist at statistically significant levels (Schwarz et al. 2016). Two are of direct relevance to the present work.

#### 1.2.1. The Cold Spot

The CMBR Cold Spot, discovered by Vielva et al. (Vielva et al. 2004) in WMAP data using a spherical Mexican-hat wavelet analysis, is a region of anomalously low temperature in the southern celestial hemisphere centred at Galactic coordinates  $(l, b) = (207.8^\circ, -56.3^\circ)$ . Its key observational characteristics are:

- Angular radius:  $\approx 5^\circ$  (corresponding to  $\sim 300$  Mpc at  $z \approx 1$ );
- Temperature decrement:  $\Delta T \approx -70 \mu\text{K}$  relative to the mean;
- Probability of occurrence in a Gaussian  $\Lambda$ CDM universe:  $\lesssim 1\text{--}2\%$  (Cruz et al. 2005).

#### 1.2.2. The Axis of Evil

The *Axis of Evil* refers to the unexpected alignment of the quadrupole and octupole moments of the CMBR with the ecliptic plane and the direction of the CMB dipole (de Oliveira-Costa et al. 2004).

This alignment is statistically anomalous at the  $\gtrsim 2\sigma$  level and has resisted complete explanation in terms of known systematic effects (Tegmark et al. 2003).

### 1.3. Theoretical Landscape

Proposed explanations for the Cold Spot fall into several categories:

- (i) **Void structure:** A large underdense region (supervoid) along the line of sight generates a temperature decrement through the Integrated Sachs–Wolfe (ISW) effect (Bremer et al. 2010; Inoue and Silk 2006; Nadathur et al. 2014).
- (ii) **Cosmic texture:** A remnant topological defect from a phase transition in the early universe imprints a characteristic non-Gaussian temperature pattern (Cruz et al. 2007; Vielva 2010).
- (iii) **Bubble collision:** A collision between our bubble universe and a neighbouring bubble in an eternally inflating landscape leaves a circular imprint in the CMBR (Feeney et al. 2011; Osborne et al. 2013).
- (iv) **Parallel universe contact:** The relic collision or early-time entanglement of our universe with a conjugate universe washes radiation away from the contact region, producing the supervoid (?).

The present paper elaborates and formalises scenario (iv), constructing a complete mathematical framework that is consistent with the observational data and makes several testable predictions.

### 1.4. Outline of the Paper

The paper is structured as follows. Section 2 introduces the two-dimensional imaginary time topology. Section 3 develops the contour-integral formalism and derives the affine parameter  $\pi$ . Section 4 establishes the entanglement–entropy framework. Section 5 connects the twin-universe split to Ricci-flow surgery. Section 6 analyses the junction via Jacobi fields. Section 7 situates the scenario within eternal inflation. Section 8 develops the holomorphic domain picture of time. Section 9 treats non-Gaussian cosmic textures. Section 10 presents the simulation-glitch matrix. Sections 12 and 13 address psychological phenomena (déjà vu and the Mandela effect). Section 14 provides the statistical analysis of conjugate universe counting. Section 15 discusses observational predictions, and Section 17 concludes.

## 2. Two-Dimensional Imaginary Time Topology

### 2.1. Motivation: From One to Two Temporal Dimensions

Standard general relativity describes spacetime as a four-dimensional Lorentzian manifold  $(\mathcal{M}, g_{\mu\nu})$  with a single time dimension. Hartle and Hawking’s no-boundary proposal (Hartle and Hawking 1983) famously employed *Euclidean time* (Wick rotation  $t \rightarrow -i\tau$ ) to regularise the path integral over geometries, effectively rendering the temporal dimension compact and imaginary near the initial singularity. The present work pursues an extension of this idea by positing that the imaginary part of time is not a mere computational convenience but a genuinely extra, hidden temporal dimension that is suppressed in the present epoch through spontaneous symmetry breaking.

**Definition 1** (Two-Dimensional Complex Time). *Let  $\mathcal{T} = \mathbb{R}^2$  denote a two-dimensional real vector space. We promote the temporal coordinate to a complex variable*

$$T = \tau + i\tilde{\tau}, \quad (4)$$

where  $\tau \in \mathbb{R}$  is the observable (real) time coordinate experienced in the  $3 + 1$ -dimensional universe, and  $\tilde{\tau} \in \mathbb{R}$  is the hidden imaginary temporal coordinate. Locally the time sector of spacetime is isomorphic to  $\mathbb{C}^1 \cong \mathbb{R}^2$ .

The physical content of this definition is that time is a closed curve in  $\mathbb{R}^2$  rather than a straight line in  $\mathbb{R}^1$ . This is analogous to the compactification of spatial dimensions in Kaluza–Klein theories, but applied to the time sector.

## 2.2. The $\mathbb{R}^2$ Closed Curves Embedded in $\mathbb{R}^3$

We model the two conjugate universes  $\alpha$  and  $\beta$  as three-dimensional Riemannian manifolds, each carrying a boundary equipped with a two-dimensional closed time curve. Formally:

- **Universe  $\alpha$ :** carries time curve  $C^1 \subset \partial\mathcal{M}_\alpha$ , a smooth closed curve in  $\mathbb{R}^2$  traversed counterclockwise (positive orientation).
- **Universe  $\beta$ :** carries time curve  $C^2 \subset \partial\mathcal{M}_\beta$ , a smooth closed curve in  $\mathbb{R}^2$  traversed clockwise (negative orientation).

The temporal parametrisation of the two universes is given by:

$$\alpha = (e^{it})_1 = (\cos t + i \sin t)_1, \quad (5)$$

$$\beta = (e^{-it})_2 = (\cos t - i \sin t)_2. \quad (6)$$

Here  $\cos t$  represents the real (observable) temporal dimension common to both universes, while  $\pm i \sin t$  encodes the imaginary temporal component running forward in  $\alpha$  and *backward* in  $\beta$ . This anti-parallel orientation is the mathematical realisation of the physically appealing notion that time runs in opposite senses in conjugate universes.

For a collection of  $n$  universes the generalisation reads:

$$\prod_{n=1}^{\infty} (e^{it})_n, \quad (7)$$

subject to the constraint that for each  $n > 1$  the orientation of the time curve is opposite to that of  $n = 1$ . The resulting contour is:

$$\Gamma = \sum_{n=1}^{\infty} \lambda_n, \quad (8)$$

where each  $\lambda_n$  is a smooth closed curve with identified endpoints  $\rho(a) = \rho(b)$ .

## 2.3. Physical Implications of Opposite Time Orientations

The most immediate physical consequence of (5) and (6) is the *arrow of time*. In our universe  $\alpha$ , the imaginary part  $+i \sin t$  grows positively with  $t$ , which corresponds to the conventional forward direction of increasing entropy. In the conjugate universe  $\beta$ , the imaginary part  $-i \sin t$  decreases with increasing  $t$ , implying that thermodynamic processes run in reverse. This is consistent with — though distinct from — the CPT-conjugate universe framework of Boyle et al. (Boyle et al. 2018), and with the two-time-dimension framework of Bars and Terning (Bars and Terning 2010).

A second consequence concerns *quantum measurement*. The imaginary time component governs the analytic continuation of quantum field theory to Euclidean space. If the imaginary parts of the two universes are opposite in sign, then quantum vacuum fluctuations at the junction  $J$  between the universes are coherently opposite, leading to destructive interference that manifests as an effective radiation drain — precisely the cold void observed in the CMBR.

## 2.4. Topological Structure: $\mathbb{R}^2$ Embedded in $\mathbb{R}^3$

The two-dimensional time surface has co-dimensionality one relative to the  $\mathbb{R}^3$  spatial topology. In embedding theory language,  $C^1$  and  $C^2$  are codimension-one submanifolds of  $\mathbb{R}^3$ . Their union, joined at the junction point  $J$ , forms a closed contour loop:

$$C^1 \cup_J C^2 = \text{closed contour of imaginary time.} \quad (9)$$

The hidden nature of this  $\mathbb{R}^2$  topology arises because the co-dimensionality of  $\mathbb{R}^2$  in  $\mathbb{R}^3$  makes it invisible to any measurement that is confined to the  $\mathbb{R}^3$  hypersurface. This is analogous to the way in which extra compact spatial dimensions are invisible to low-energy observers.

### 3. Contour-Integral Formalism and the Affine Parameter $\pi$

#### 3.1. Contour Integrals on the Time Curves

Having established the geometry of the time curves, we now compute the contour integrals that govern the dynamics of the junction between the two universes. These integrals arise naturally from the requirement that the time-evolution operators on  $C^1$  and  $C^2$  are mutually consistent across the junction.

Setting  $\rho(t) = e^{it}$ , the basic contour integral over  $C^1$  (counterclockwise) is:

$$\oint_{C^1} \frac{1}{\rho} d\rho = \int_0^{2\pi} \frac{1}{e^{it}} ie^{it} dt = i \int_0^{2\pi} dt = 2\pi i. \quad (10)$$

Over  $C^2$  (clockwise, i.e. limits reversed):

$$\oint_{C^2} \frac{1}{\rho} d\rho = \int_{2\pi}^0 \frac{1}{e^{it}} ie^{it} dt = -2\pi i. \quad (11)$$

Equations (10) and (11) encode the opposite orientations of the two time curves:

$$2\pi i \xrightarrow{\text{opposite orientations}} -2\pi i. \quad (12)$$

#### 3.2. The Affine Parameter Integral

To extract a real-valued affine parameter for the combined contour, we consider the integral:

$$I = \int_{-\pi}^{\pi} \frac{1}{1 + 3(\cos t)^2} dt. \quad (13)$$

Substituting  $\rho = e^{it}$ , so that  $\cos t = \frac{1}{2}(\rho + \rho^{-1})$  and  $dt = d\rho/(i\rho)$ , we obtain:

$$I = \oint_{|\rho|=1} \frac{1}{1 + \frac{3}{4}(\rho + \rho^{-1})^2} \cdot \frac{d\rho}{i\rho}. \quad (14)$$

Expanding the denominator:

$$1 + \frac{3}{4}\left(\rho + \frac{1}{\rho}\right)^2 = 1 + \frac{3}{4}(\rho^2 + 2 + \rho^{-2}) = \frac{3\rho^4 + 10\rho^2 + 3}{4\rho^2}. \quad (15)$$

Therefore:

$$I = \oint_C \frac{-4i}{3\rho^4 + 10\rho^2 + 3} \cdot \rho d\rho = -4i \oint_C \frac{\rho}{3\rho^4 + 10\rho^2 + 3} d\rho. \quad (16)$$

Factoring the denominator:

$$3\rho^4 + 10\rho^2 + 3 = 3(\rho + \sqrt{3}i)(\rho - \sqrt{3}i)\left(\rho + \frac{i}{\sqrt{3}}\right)\left(\rho - \frac{i}{\sqrt{3}}\right). \quad (17)$$

The poles inside the unit disc  $|\rho| = 1$  are at  $\rho = \pm i/\sqrt{3}$  (since  $|i/\sqrt{3}| = 1/\sqrt{3} < 1$ , while  $|\sqrt{3}i| = \sqrt{3} > 1$ ). Applying the residue theorem separately over  $C^1$  (enclosing  $\rho = +i/\sqrt{3}$ ) and  $C^2$  (enclosing  $\rho = -i/\sqrt{3}$ ):

**Theorem 1** (Affine Parameter Theorem). *The sum of contour integrals of the meromorphic function  $f(\rho) = \rho/[3(\rho + \sqrt{3}i)(\rho - \sqrt{3}i)(\rho + i/\sqrt{3})(\rho - i/\sqrt{3})]$  over the oppositely oriented unit circles  $C^1$  and  $C^2$  is:*

$$-\frac{4i}{3} \left[ 2\pi i \operatorname{Res}\left(f, \frac{i}{\sqrt{3}}\right) + 2\pi i \operatorname{Res}\left(f, -\frac{i}{\sqrt{3}}\right) \right] = \pi. \quad (18)$$

**Proof.** The residue at  $\rho_0 = i/\sqrt{3}$  is:

$$\text{Res}\left(f, \frac{i}{\sqrt{3}}\right) = \frac{i/\sqrt{3}}{\left(\frac{i}{\sqrt{3}} + \sqrt{3}i\right)\left(\frac{i}{\sqrt{3}} - \sqrt{3}i\right) \cdot \frac{4i}{\sqrt{3}} \cdot 3} = \frac{i/\sqrt{3}}{\frac{4i}{\sqrt{3}} \cdot \left(-\frac{2i}{\sqrt{3}}\right) \cdot \frac{2i}{\sqrt{3}} \cdot 3} = \frac{3}{16}. \quad (19)$$

By symmetry  $\text{Res}(f, -i/\sqrt{3}) = 3/16$ . Hence:

$$-\frac{4i}{3} \left[ 2\pi i \cdot \frac{3}{16} + 2\pi i \cdot \frac{3}{16} \right] = -\frac{4i}{3} \cdot 2\pi i \cdot \frac{3}{8} = -\frac{4i}{3} \cdot \frac{3\pi i}{4} = \pi.$$

□

The value  $\pi$  plays the role of an *affine parameter* for the coupled system of the two universes. It can be interpreted as the angle subtended by each of the two time loops when they are merged into a single closed contour, consistent with the topological picture of two circles joined at a point.

### 3.3. The Vanishingly Small Loop Limit

Combining the two opposite-orientation results, the net loop has diameter  $2R$  with:

$$\lim_{R \rightarrow 0^+} 2\pi R = 0, \quad (20)$$

which represents the epoch at  $t = 0$  (the Big Bang) when the two universes occupied the same infinitesimal volume. As the universe inflates and expands,  $R$  grows, pulling the two time curves apart and leaving behind the Cold Spot as a relic of their former contact.

## 4. Entanglement Entropy of Conjugate Universes

### 4.1. Vacuum Landscape and Initial Conditions

Within the eternal inflation paradigm, the string landscape contains approximately  $\mathcal{N} \sim 10^{500}$  metastable vacuum states (Bousso and Polchinski 2000; Susskind 2003). The Cold Spot, as observed by WMAP (Hinshaw et al. 2013) and the Sloan Digital Sky Survey (Granett et al. 2008), spans roughly 900 million light-years, which is far too large to be a statistical fluctuation in the single-universe  $\Lambda$ CDM model.

At the split-second after the Big Bang, when the linear dimension of the universe was of order (20), quantum vacuum fluctuations at the intersection region of the two time curves  $C^1$  and  $C^2$  were immense. These fluctuations gave rise to:

- (i) A single composite loop of imaginary time from the merger of the two opposite-orientation loops;
- (ii) Negative pressure domination (analogous to the Casimir effect) at the junction  $J$ ;
- (iii) Repulsive effective gravity in the junction region, leading to radiation evacuation.

As the universe expanded, the junction region grew with it, eventually manifesting as the observed supervoid with its anomalously low star density and radiation temperature.

### 4.2. Quantum State of the Universe Pair

We model each universe as a quantum system with a Hilbert space  $\mathcal{H}_\alpha$  and  $\mathcal{H}_\beta$  respectively. The temporal state of universe  $\alpha$  is:

$$|(e^{it})_{C^1}\rangle_\alpha \quad (21)$$

and of universe  $\beta$ :

$$|(e^{-it})_{C^2}\rangle_\beta. \quad (22)$$

The combined state before separation is a pure state in  $\mathcal{H}_\alpha \otimes \mathcal{H}_\beta$ :

$$|\Psi\rangle_{\alpha\beta} = \sum_{i,j} e^{ij} |i\rangle_\alpha \otimes |j\rangle_\beta, \quad (23)$$

where  $|i\rangle_\alpha$  and  $|j\rangle_\beta$  are orthonormal bases for the respective Hilbert spaces, and  $e^{ij}$  are expansion coefficients satisfying  $\sum_j |e^{ij}|^2 = 1$ .

Associating the orientations  $2\pi i$  and  $-2\pi i$  with the computational basis states  $|0\rangle$  and  $|1\rangle$  respectively, the maximally entangled (Bell-like) state is:

$$|\Psi\rangle_{\alpha\beta} = \frac{1}{\sqrt{2}}(|0\rangle_\alpha \otimes |1\rangle_\beta - |1\rangle_\alpha \otimes |0\rangle_\beta). \quad (24)$$

This is precisely the spin-singlet Bell state, which is maximally entangled: no local operation on  $\alpha$  alone can influence the state of  $\beta$ , yet measurements on the two systems are maximally correlated.

#### 4.3. Density Matrix and von Neumann Entropy

The full density matrix of the two-universe system is:

$$\epsilon = \sum_{i,j} \gamma_i \left[ \sum_j e_{ij} |ij\rangle_\alpha \otimes |ij\rangle_\beta \right] \left[ \sum_k \bar{e}_{ik} \langle ik|_\alpha \otimes \langle ik|_\beta \right], \quad (25)$$

with the normalisation  $\sum_j |e_{ij}|^2 = 1$ . The maximally entangled state corresponds to the reduced density matrix being proportional to the identity:

$$\epsilon_{\text{red}} = \begin{pmatrix} 1/n & & \\ & \ddots & \\ & & 1/n \end{pmatrix}, \quad (26)$$

where  $n$  is the dimension of the Hilbert space for each universe.

The *von Neumann entropy* of entanglement is:

$$S(\epsilon) = -\text{Tr}(\epsilon \log_2 \epsilon) = -\sum_i \epsilon_i \log_2 \epsilon_i \Big|_{\epsilon \neq 0}, \quad (27)$$

which achieves its maximum value  $S_{\text{max}} = \log_2 n$  when all eigenvalues  $\epsilon_i = 1/n$ . For the Bell state (24), the eigenvalues are  $\epsilon_i = 1/2$ , giving  $S = 1$  ebit.

#### 4.4. Time Evolution and Entropy Growth

The temporal evolution operator connecting the early-time (attached) state to the late-time (separated) state is:

$$T(t, t_1) = \exp\left(\frac{-iH(t, t_1)}{\hbar}\right), \quad t_1 \gg t, \quad (28)$$

where  $H$  is the Hamiltonian governing the joint dynamics. The entropy of the evolved density matrix satisfies:

$$S(\epsilon) = S(T_\epsilon T^*), \quad (29)$$

where  $T^*$  is the complex-conjugate evolution operator, corresponding physically to the backward-time evolution in universe  $\beta$ . As  $t_1 \rightarrow \infty$ , the entropy  $S(\epsilon) \rightarrow S_{\text{max}}$ , meaning the two universes become maximally entangled even as they become spatially separated — a manifestation of quantum non-locality at cosmological scales.

#### 4.5. Temporal Operator and Entanglement Tensor Product

The temporal state operator for the joint system is:

$$(e^{it})_{C^1} \otimes (e^{-it})_{C^2}, \quad (30)$$

implying:

$$|(e^{it})_{C^1}\rangle_\alpha \otimes |(e^{-it})_{C^2}\rangle_\beta. \quad (31)$$

This tensor product structure is the hallmark of quantum entanglement: neither universe is in a definite state independently; rather the state is a holistic property of the pair. The entropy–entanglement relation is:

$$S_{\text{entanglement}} = \log_2 \epsilon, \quad \epsilon \neq 0. \quad (32)$$

## 5. Ricci Flow, Singularity, and the Universal Split

### 5.1. Poincaré Conjecture and Topological Surgery

The mechanism by which a single parent manifold splits into two child universes can be made mathematically precise using Perelman’s proof of the Poincaré conjecture via Ricci flow with surgery (Perelman 2002, 2003a,b). The key idea is that a compact, simply connected Riemannian 3-manifold, evolved under the Ricci flow:

$$\partial_t g_{ij} = -2R_{ij}, \quad (33)$$

will develop singularities in finite time. These singularities correspond geometrically to regions of extreme positive curvature, and topologically they signal the *necking* of the manifold — the formation of a narrow neck that eventually pinches off, separating the manifold into two components.

### 5.2. Curvature Singularities and Blow-Up

Let  $(M, g(t))$  be a Ricci flow solution on the time interval  $t \in [0, T)$  with  $T < \infty$ . The Riemann curvature norm  $|\mathbf{Rm}|$  blows up as  $t \rightarrow T$ :

$$K_i := |\mathbf{Rm}(g_{t_i})|(p_i) \rightarrow \infty \quad \text{as } i \rightarrow \infty, \quad (34)$$

for a sequence of space-time points  $(p_i, t_i) \in M \times [0, T)$ . Under parabolic rescaling:

$$g_i(t) = K_i g\left(t_i + \frac{t}{K_i}\right), \quad t \in [-K_i t_i, 0], \quad (35)$$

the rescaled metric satisfies the Ricci flow equation with bounded curvature  $|\mathbf{Rm}| \leq K_i$  on  $M \times [t_i, 0]$ . By Hamilton’s compactness theorem (Hamilton 1995), the sequence  $(M, g_i(t), p_i)$  subconverges to a limiting *ancient* Ricci flow:

$$\langle M_\infty, g_\infty(t), p_\infty \rangle, \quad (36)$$

which has non-negative sectional curvature and represents the local geometry near the singularity.

### 5.3. Topological Surgery and Twin Universe Birth

At the singularity time  $t = T$ , Perelman’s surgery procedure removes a tubular neighbourhood of the neck (a region diffeomorphic to  $S^2 \times (-1, 1)$ ), caps each end with a hemisphere, and continues the Ricci flow. The result is that the original manifold  $M$  is replaced by two disjoint manifolds  $M_1$  and  $M_2$ , each with positive sectional curvature. In the cosmological context:

- $M$  represents the parent universe at the Big Bang epoch;
- $M_1 \cong S^3$  represents our observable universe;
- $M_2 \cong S^3$  represents the conjugate parallel universe.

The codimension of the quotient spaces is determined by:

$$\text{codim}(Q) = \dim(V/Q) = \dim(V) - \dim(Q), \quad (37)$$

$$\text{codim}(U) = \dim(V/U) = \dim(V) - \dim(U). \quad (38)$$

Equating (37) and (38):

$$\dim(Q) = \dim(U), \quad (39)$$

which expresses the *dimensional democracy* of the two child universes: if the parent space  $V$  has dimension  $d$ , then the two quotient spaces  $V/Q$  and  $V/U$  have the same dimension, ensuring the twin universes are topologically equivalent.

Introducing the split operator  $\aleph$  with probability factor  $\aleph^{*2} = 1$  and junction  $J$  between the two child universes:

$$\left\langle \begin{matrix} Q \\ U \end{matrix} \left\langle R_{C_1 + \frac{i}{\sqrt{3}}}^2 \right\rangle \stackrel{J}{\Leftrightarrow} R_{C_2 - \frac{i}{\sqrt{3}}}^2 \right\rangle \aleph^{*2}, \quad (40)$$

where:

$$\aleph^{*2} = \frac{1}{\mathcal{F}}(U \oplus Q), \quad \mathcal{F} \in \mathbb{R}. \quad (41)$$

This yields:

$$\frac{1}{\mathbb{N}}(U \oplus Q) \quad \text{and} \quad \frac{1}{\mathcal{M}}(U \oplus Q), \quad \exists \mathcal{M}, \mathbb{N} \in \mathbb{R}, \quad \mathcal{M} \neq \mathbb{N}. \quad (42)$$

## 6. Jacobi Fields and Junction Analysis

### 6.1. Geodesics on the Time-Curve Manifold

On the two-dimensional time surface (modelled as a 2-sphere of positive curvature), every great circle is a geodesic. Consider the Riemann manifold  $(M, g)$  with metric  $g$  and Riemann tensor:

$$R^k_{ij\ell} = \frac{\partial}{\partial x^i} \Gamma^k_{j\ell} - \frac{\partial}{\partial x^\ell} \Gamma^k_{ij} + \Gamma^m_{i\ell} \Gamma^k_{mj} - \Gamma^m_{ij} \Gamma^k_{m\ell}. \quad (43)$$

The associated Ricci tensor and Ricci scalar are:

$$R_{j\ell} = g^i_k R^k_{ij\ell} \neq 0, \quad (44)$$

$$R = g^j_\ell R_{j\ell} \neq 0. \quad (45)$$

The Kretschmann scalar:

$$\mathcal{K} = R^{\mu\nu\lambda\kappa} R_{\mu\nu\lambda\kappa} \quad (46)$$

takes the following values on the spherical geometry:

$$\mathcal{K} \neq 0 \quad (\text{on the sphere}), \quad (47)$$

$$\mathcal{K} \gg 0 \quad (\text{positive curvature, outer surface}), \quad (48)$$

$$\mathcal{K} \ll 0 \quad (\text{negative curvature, inner surface}). \quad (49)$$

### 6.2. Geodesic Equations

For a closed geodesic  $\gamma : \mathbb{R} \rightarrow M$  the action is:

$$S(\gamma) = \int_a^b g(\gamma)_t(\dot{\gamma}(t), \dot{\gamma}(t)) dt, \quad a \equiv b, \quad (50)$$

whose Euler–Lagrange equations (for a smooth manifold with affine connection  $\nabla$ ) are the geodesic equations:

$$\nabla_{\dot{\gamma}} \dot{\gamma} = 0, \quad (51)$$

$$\frac{d^2 \gamma^\lambda}{dt^2} + \Gamma^\lambda_{\mu\nu} \frac{d\gamma^\mu}{dt} \frac{d\gamma^\nu}{dt} = 0. \quad (52)$$

The junction condition between  $C^1$  and  $C^2$  can be written as:

$$R_{C_1}^2 \stackrel{J}{\Leftrightarrow} R_{C_2}^2 \equiv \left. \frac{d^2 \gamma^\lambda}{dt^2} + \Gamma^\lambda_{\mu\nu} \frac{d\gamma^\mu}{dt} \frac{d\gamma^\nu}{dt} \right\}_J \text{ as Points of Intersection.} \quad (53)$$

### 6.3. Jacobi Fields and the Six Buffer Points

For two intersecting geodesics with tangent vectors  $u$  and  $x$ , the geodesic deviation equation is:

$$(\nabla_u \nabla_u x)^a = -R^k{}_{ij\ell} u^i x^j u^\ell. \quad (54)$$

The Jacobi field equations along the two geodesics  $\gamma_\tau$  are:

$$u(t) = \left. \frac{\partial \gamma_\tau(t)}{\partial \tau} \right|_{\tau=0}, \quad (55)$$

$$x(t) = \left. \frac{\partial \gamma_\tau(t)}{\partial \tau} \right|_{\tau=0}, \quad (56)$$

$$\frac{\nabla^2}{dt} u(t) + R(u(t), \dot{\gamma}(t), \dot{\gamma}(t)) = 0, \quad (57)$$

$$\frac{\nabla^2}{dt} x(t) + R(x(t), \dot{\gamma}(t), \dot{\gamma}(t)) = 0. \quad (58)$$

For a Riemannian manifold of constant positive curvature  $K > 1$ , any Jacobi field is a linear combination of  $\dot{\gamma}(t)$ ,  $t\dot{\gamma}(t)$ ,  $\sin(kt) e_i(t)$ ,  $\cos(kt) e_i(t)$  for  $i > 1$ . This gives six possible intersection configurations for the two time curves  $C^1$  and  $C^2$  at the junction  $J$ , labelled by buffer-point parameters  $\beta_0, \dots, \beta_5$ :

$$\begin{aligned} A' R_{C_1}^2 \overset{J\beta_0}{\leftrightarrow} R_{C_2}^2 S', & \quad A'' R_{C_1}^2 \overset{J\beta_1}{\leftrightarrow} R_{C_2}^2 S'', \\ A' R_{C_1}^2 \overset{J\beta_2}{\leftrightarrow} R_{C_2}^2 A'', & \quad S' R_{C_1}^2 \overset{J\beta_3}{\leftrightarrow} R_{C_2}^2 S'', \\ A' R_{C_1}^2 \overset{J\beta_4}{\leftrightarrow} R_{C_2}^2 S'', & \quad S' R_{C_1}^2 \overset{J\beta_5}{\leftrightarrow} R_{C_2}^2 A''. \end{aligned} \quad (59)$$

The geodesic distance between two nearby geodesics  $\gamma_\tau^0$  and  $\gamma_\tau^1$  separated by angle  $\tau$ , with  $t \in [0, \pi]$ , is:

$$d(\gamma_\tau^0(t), \gamma_\tau^1(t)) = \arcsin\left(\sin(t) \sin(\tau) \sqrt{1 + \cos^2(t) \tan^2\left(\frac{\tau}{2}\right)}\right) \equiv J. \quad (60)$$

The existence of the six buffer points (59) implies that there are six distinct temporal channels through which the moment of time can flow between the two universes, providing a microscopic mechanism for inter-universe quantum correlations.

## 7. Eternal Inflation and the Multiverse

### 7.1. Hubble Expansion and Recession Velocity

The kinematic foundation of the expanding universe is Hubble's law:

$$v = H_0 D, \quad (61)$$

where  $v$  is the recession velocity of a distant galaxy,  $D$  is the comoving distance, and  $H_0$  is the Hubble constant. The Planck 2018 measurement gives  $H_0 = 67.4 \pm 0.5 \text{ km s}^{-1} \text{ Mpc}^{-1}$  (Planck Collaboration 2020), while local distance-ladder measurements yield  $H_0 \approx 73 \text{ km s}^{-1} \text{ Mpc}^{-1}$  (Riess et al. 2022) — the Hubble tension.

### 7.2. Eternal Inflation

In the eternal inflation scenario (Guth 1981, 2007; Linde 1986; Vilenkin 1983), the inflaton field undergoes quantum fluctuations that continuously regenerate inflationary regions faster than they can thermalize. The key features are:

- (i) Most of the universe at any given time is still inflating;
- (ii) Thermalized (bubble) universes nucleate within the inflating background;
- (iii) The process is eternal to the future: an everlasting multiverse is produced;

(iv) Each bubble universe is itself infinite and has its own local physical constants.

A single parent bubble can give rise to child bubbles through the process of false-vacuum decay. If a parent space  $V$  over field  $K$  contains a subspace  $Q$ , then  $V \bmod Q$  gives a quotient space  $U$  with:

$$V = U \oplus Q, \quad (62)$$

$$V / Q \cong U. \quad (63)$$

The epimorphism  $f : V \rightarrow V/Q$  sends  $x \mapsto [x] = x + N$ . This gives the twin universe identity: both quotients  $V/Q$  and  $V/U$  have the same dimension (39), ensuring the two child universes are topological twins.

### 7.3. Self-Reproduction and Exponential Growth

The eternal inflation model predicts a self-reproducing structure in which each inflating domain  $\mathcal{D}$  of Hubble volume  $V_H$  gives birth to approximately  $e^{3H\Delta t}$  new inflationary domains in each time step  $\Delta t$ . This leads to exponential growth in the number of universes:

$$\mathcal{N}(t) \sim e^{3Ht}, \quad (64)$$

consistent with the landscape estimate of  $10^{500}$  vacua (Bousso and Polchinski 2000).

The entropic evolution of the multiverse can be described by the affine variable:

$$\zeta = \prod_{i=1}^{\infty} \gamma_i, \quad (65)$$

representing the infinite possibilities for universe creation. The two-point split function for the parent-child relationship is:

$$f(\sigma) = \begin{cases} x = -y, & y < 0 \\ x = y, & y > 0 \end{cases} \quad (\text{Point 1: single separation}), \quad (66)$$

$$f(\sigma) = \begin{cases} y = \sin(x), & x > 0 \\ y = -\sin(x), & x < 0 \end{cases} \quad (\text{Point 2: sinusoidal encounters}). \quad (67)$$

Point 1 describes a universe pair that separates permanently after the Big Bang, producing a single cold spot. Point 2 describes a scenario in which the two universes undergo periodic encounters (at the nodes of the sinusoidal trajectory), each encounter producing a cold spot. The fact that only one cold spot is observed in the current epoch supports Point 1, or equivalently, that the universe is too young to have experienced a second encounter under Point 2.

## 8. Holomorphic Domain of Time

### 8.1. Pre- and Post-Big Bang Time

The spontaneous symmetry breaking that converted imaginary time into real time can be modelled as a phase transition through the following sequence of domains:

$$\bar{D} \rightarrow \overline{Sp} \rightarrow D, \quad (68)$$

where:

$$\bar{D} \approx \text{Time before Big Bang (imaginary time)}, \quad (69)$$

$$\bar{S}p \approx \text{Spontaneous symmetry breaking (Big Bang)}, \quad (70)$$

$$D \approx \text{Time after Big Bang (real time)}. \quad (71)$$

Formally,  $\bar{D} = iD$ , so that:

$$T = D + \bar{D} = \tau + i\tau, \quad (72)$$

which recovers the complex time definition (4). The symmetry breaking potential is:

$$\bar{S}p = \partial^\nu \varphi \partial_\nu \varphi - |\varphi|^4 + 10|\varphi|^2, \quad \varphi = \sqrt{5} e^{i\theta}, \quad \theta \in [0, 2\pi), \quad (73)$$

which has a Mexican-hat shape with a ring of minima at  $|\varphi| = \sqrt{5}$ . The false vacuum at  $\varphi = 0$  transitions to the true vacuum ring, and in doing so the imaginary component of time becomes hidden.

### 8.2. Holomorphic Functions of Complex Time

The temporal dimension is described as:

$$f(\eta) : \mathbb{C}^n, \quad n = 1, \quad (74)$$

which is isomorphic to  $\mathbb{R}^{2n} = \mathbb{R}^2$ , confirming that one complex time dimension behaves as two real dimensions. The function  $f(\eta)$  is continuous on  $\bar{D}$ , and for each complex variable  $T^\lambda = \tau^\lambda + i\tilde{\tau}^\lambda$ , the holomorphicity condition is:

$$\frac{\partial f}{\partial T^\lambda} = 0. \quad (75)$$

Writing  $f(T_1, \dots, T_n) = u(\tau_1, \dots, \tau_n) + iv(i\tilde{\tau}_1, \dots, i\tilde{\tau}_n)$ , the Cauchy–Riemann equations in complex time are:

$$\text{Re}\left(\frac{\partial f}{\partial T^\lambda}\right) = \frac{\partial u}{\partial \tau^\lambda} - \frac{\partial v}{\partial \tilde{\tau}^\lambda} = 0, \quad (76)$$

$$\text{Im}\left(\frac{\partial f}{\partial T^\lambda}\right) = \frac{\partial u}{\partial \tilde{\tau}^\lambda} + \frac{\partial v}{\partial \tau^\lambda} = 0, \quad (77)$$

so that:

$$\text{Re}\left(\frac{\partial f}{\partial T^\lambda}\right) = \text{Im}\left(\frac{\partial f}{\partial T^\lambda}\right). \quad (78)$$

This equality of real and imaginary parts of the temporal derivative is the mathematical signature of the holomorphic embedding of time.

### 8.3. Implications for Causality

The holomorphic structure of time has profound implications for causality. In the pre-Big Bang domain  $\bar{D}$ , time is purely imaginary ( $\tau = 0$ ), and causal ordering is undefined in the usual sense — consistent with the no-boundary proposal. In the post-Big Bang domain  $D$ , time is purely real ( $\tilde{\tau} = 0$ ), and the standard causal structure of Lorentzian spacetime is recovered. The spontaneous symmetry breaking at  $\bar{S}p$  marks the transition from acausal (quantum gravity) to causal (classical cosmology) dynamics.

The imaginary component  $\tilde{\tau}$  persists as a hidden degree of freedom in the post-Big Bang epoch, and it is this hidden component that is responsible for the junction points, the entanglement between the universes, and ultimately the observable anomalies in the CMBR.

## 9. Non-Gaussian Cosmic Textures

### 9.1. Topological Defects in the Early Universe

Cosmic textures are non-singular topological defects that arise when a global symmetry group  $G$  is spontaneously broken to a subgroup  $H$  such that the third homotopy group  $\pi_3(G/H)$  is non-trivial (Davis and Shellard 1987; Turok 1990). Unlike monopoles or strings, textures are unstable and collapse on the light-crossing timescale, releasing their energy as a burst of scalar radiation that leaves a characteristic hot or cold imprint on the CMBR.

### 9.2. Temperature Fluctuation from a Cosmic Texture

The temperature fluctuation induced by a collapsing texture of amplitude  $\epsilon$  and angular size  $\vartheta$  is (Cruz et al. 2007; Vielva 2010):

$$\frac{\Delta T}{T} = \pm \begin{cases} \frac{\epsilon}{\sqrt{1 + 4\left(\frac{\vartheta}{\vartheta_c}\right)^2}}, & \vartheta \leq \vartheta_* \\ \frac{\epsilon}{2} \exp\left[-\frac{1}{2\vartheta_c^2}(\vartheta^2 + \vartheta_*^2)\right], & \vartheta > \vartheta_* \end{cases} \quad (79)$$

and for  $\vartheta > \vartheta_*$ :

$$\frac{\Delta T}{T} = \pm \left\{ \frac{\epsilon}{2} \exp\left[-\frac{1}{2\vartheta_c^2}(\vartheta^2 + \vartheta_*^2)\right] \right\}. \quad (80)$$

Here the parameters for the Cold Spot are (Vielva 2010):

$$\vartheta = 5^\circ, \quad \epsilon = 10^{-4}, \quad \vartheta_* = \frac{\sqrt{3}}{2} \vartheta_c. \quad (81)$$

### 9.3. Bayesian Evidence for the Texture Hypothesis

Given a data set  $\mathcal{E}$  and unknown parameters  $\Theta$  for hypothesis  $\mathfrak{H}_i$ , Bayes' theorem gives:

$$P(\Theta|\mathcal{E}, \mathfrak{H}_i) = \frac{P(\mathcal{E}|\Theta, \mathfrak{H}_i) P(\Theta|\mathfrak{H}_i)}{P(\mathcal{E}|\mathfrak{H}_i)}, \quad (82)$$

where the normalisation constant (Bayesian evidence) is:

$$P(\mathcal{E}|\mathfrak{H}_i) = \int P(\mathcal{E}|\Theta, \mathfrak{H}_i) P(\Theta|\mathfrak{H}_i) d\Theta. \quad (83)$$

The posterior ratio (Bayes factor) comparing the texture hypothesis  $\mathfrak{H}_1$  to the Gaussian null hypothesis  $\mathfrak{H}_0$  is:

$$\beta_\rho \equiv \frac{P(\mathfrak{H}_1|\mathcal{E})}{P(\mathfrak{H}_0|\mathcal{E})} = \frac{D_1}{D_0} \cdot \frac{P(\mathfrak{H}_1)}{P(\mathfrak{H}_0)}. \quad (84)$$

From the WMAP data, the marginalisation of the posterior over texture parameters yields (Cruz et al. 2007):

$$\epsilon = 7.3_{-3.6}^{+2.5} \times 10^{-5}, \quad \vartheta = 4.9_{-2.4}^{+2.8} \text{ at } 95\% \text{ confidence}, \quad (85)$$

with a Bayes factor  $\beta_\rho \approx 150$ , constituting very strong evidence for the texture hypothesis. The Cold Spot spans  $\approx (0.017)$  sr, and the posterior ratio at this scale is  $\beta_\rho \approx 2.5$ .

### 9.4. Reconciling the Texture and Parallel Universe Hypotheses

The texture and parallel universe interpretations of the Cold Spot are not mutually exclusive. In fact, they complement each other: a cosmic texture could represent the topological remnant of the symmetry-breaking junction  $J$  between our universe and its conjugate, precisely at the location where

the two  $R^2$  time curves were last in contact. The texture amplitude  $\epsilon \sim 10^{-4}$ – $10^{-5}$  then provides a direct measure of the coupling strength between the two universes.

## 10. Glitch Matrix and Simulated Reality

### 10.1. The Simulation Hypothesis

The simulation argument (Bostrom 2003a,b, 2008) posits that if a sufficiently advanced civilisation can run high-fidelity simulations of entire universes, and if there are many such civilisations in the multiverse, then the probability that any given observer is in a “base reality” is negligibly small. In the framework of the present paper, the NP (non-polynomial) complexity of the multiverse — arising from the exponential growth of entangled universe states — naturally produces glitches analogous to software errors.

### 10.2. The Glitch Exponential

The junction conditions between the two universes are encoded in the mapping factor  $A^*$ :

$$R^2 \stackrel{J}{\leftrightarrow} R^2 \rightarrow R_{C_1}^2 \stackrel{J}{\leftrightarrow} R_{C_2}^2, \quad (86)$$

$$A^* : \partial 2\pi i \rightarrow -\partial 2\pi i \rightarrow \partial 2\pi i \rightarrow -\partial 2\pi i \dots \quad (87)$$

with the metric tensor:

$$\tilde{\xi}_{\mu\nu} \hat{A}^{*\mu} \hat{A}^{*\nu} = \begin{pmatrix} \partial 2\pi i & 0 & 0 & 0 \\ 0 & -\partial 2\pi i & 0 & 0 \\ 0 & 0 & \partial 2\pi i & 0 \\ 0 & 0 & 0 & -\partial 2\pi i \end{pmatrix}. \quad (88)$$

This matrix has vanishing trace:  $\text{Tr}(\partial 2\pi i, -\partial 2\pi i, \partial 2\pi i, -\partial 2\pi i) = 0$ .

If the term  $-\partial 2\pi i$  is Wick-rotated as  $-\partial 2\pi i \cdot i = \partial 2\pi$ , then the imaginary and negative signs cancel, yielding the fundamental domain  $\partial 2\pi$ . The NP glitch exponential is:

$$= a^{b^{c^{d^{\dots}}} \xrightarrow{\text{encoded under}} \partial 2\pi \begin{cases} \partial 2\pi i \\ -\partial 2\pi i \end{cases}, \quad (89)$$

where  $a, b, c, d, \dots$  are the consecutive layers of simulated glitches. The glitch is classified into two subgroups:

$$= \begin{cases} +, & \text{High Errors} \\ -, & \text{Low Errors} \end{cases}. \quad (90)$$

### 10.3. Critical Dimension and Holographic Principle

Assuming the universe has  $D = 10$  total dimensions, the critical codimension is:

$$D_c = \sqrt{\frac{D-2}{2}} = \sqrt{\frac{10-2}{2}} = 2, \quad (91)$$

consistent with the holographic principle (Susskind 1995): the entire 10-dimensional spacetime is projected as a hologram on a 2-dimensional screen.

### 10.4. Low Errors: Mandela Effect and Déjà Vu

Low errors ( $-$ ) manifest as minor perceptual glitches in the simulation matrix, including:

- The Mandela effect (collective false memories of historical events);
- Déjà vu (the sense of having previously experienced a novel situation);
- Confabulations (unconscious fabrication of memory).

### 10.5. High Errors: Variation of Fundamental Constants

High errors (+) would alter the fundamental constants of nature  $G$ ,  $c$ ,  $\hbar$  by one part in  $10^{13}$ . The relationship between the glitch and Planck's constant is:

$$= \hbar \cdot \partial 2\pi = \frac{h}{2\pi} \cdot \partial 2\pi \approx h, \quad (92)$$

suggesting that Planck's constant itself should be replaced by  $\partial h$  in a fully glitch-corrected simulation, where  $\partial h$  denotes the partial (layered) version of  $h$  that accommodates the error structure.

### 10.6. The Simulation Reality Equation

The complete simulation reality equation is:

$$\mathbf{S}_{\mathcal{R}} = \text{Tr}(\beta)_{\mathcal{M}|\ell} \times \mathbf{T}_f(e^x) \times \bigvee_{\gamma=1}^{g_k} \sum_{k=1}^{64} \mathcal{V}\gamma g_k \times \sqrt{\frac{D-2}{2}} \times \bigcup_{i=1, j=1}^{\infty} \psi_{I_{ij}} \left[ \begin{array}{c} a^{b^{c^d}} \\ * \\ * \end{array} \right]^{\left(\frac{1}{T_2} - \frac{1}{T_1}\right)}, \quad (93)$$

where:  $\text{Tr}(\beta)_{\mathcal{M}|\ell}$  is the timelike/spacelike trace with Minkowski metric  $\mathcal{M}$  and margin of error  $\ell$ ;  $\mathbf{T}_f(e^x)$  is the shadow of the simulation with  $x \in \{-\infty, 0, +\infty\}$ ;  $g_{64}$  is Graham's number providing the computing capacity;  $\sqrt{(D-2)/2} = 2$  is the critical holographic dimension; and the final term encodes the time-evolving glitch matrix from  $T_1$  to  $T_2$ .

## 11. Conjugate Universe Field Action

The action governing the motion of a single universe  $\mathcal{U}$  floating in the multiverse medium is denoted by the operator  $\mathbb{W}$  and is:

$$\mathbb{W} = \iiint \int |\mathcal{L}\psi \times \zeta f(\sigma)|^{\tau \pm \frac{i}{\sqrt{3}}} \Delta \mathcal{H}^c, \quad (94)$$

where:

- $\mathcal{L}$  is the Lagrangian density multiplied by all matter fields  $\psi$ ;
- $f(\sigma)$  is the split function with affine variable  $\zeta$ ;
- $\tau$  is the proper time of evolution;
- $\pm i/\sqrt{3}$  are the singularity points identified in Theorem 1;
- $\mathcal{H}^c$  represents the complex hyper-coordinates.

The affine variable  $\zeta$  encodes the possibility of infinitely many universes:

$$\zeta = \bigvee_{i=1}^{\infty} \gamma_i, \quad (95)$$

so that the action  $\mathbb{W}$  is defined for arbitrarily large cosmological configurations.

The singularity points  $\pm i/\sqrt{3}$  appearing in (94) are precisely the poles identified in the affine parameter derivation (Section 3). They mark the locations in the complex time plane at which our universe ( $+i/\sqrt{3}$ , corresponding to curve  $C^1$ ) and the conjugate universe ( $-i/\sqrt{3}$ , corresponding to curve  $C^2$ ) are anchored.

## 12. Phenomenology: Déjà Vu, Confabulation, and the Mandela Effect

### 12.1. Psychological Background

The phenomena of déjà vu, confabulation, and the Mandela effect have long challenged neuroscientists and psychologists. Despite extensive investigation, no purely neurological explanation has achieved consensus:

- Déjà vu: reported by approximately 2/3 of healthy adults (Brown 2003), with no established correlation with schizophrenia, anxiety, depression, or other psychiatric conditions (O'Connor and Moulin 2010);
- Confabulation: the unconscious fabrication of detailed, plausible false memories (Schneider 2008);
- Mandela effect: large-scale collective false memories, named for the widely shared (but false) recollection that Nelson Mandela died in prison in the 1980s, whereas he died in 2013 (?).

### 12.2. Physical Interpretation via Junction Points

In the framework developed here, the six buffer points  $\{\beta_0, \dots, \beta_5\}$  of the junction  $J$  (Section 6) constitute temporal channels through which information can leak between the two universes. When the hidden imaginary time dimension  $\tilde{\tau}$  fluctuates at one of these buffer points, an observer in universe  $\alpha$  momentarily accesses a fragment of experience from universe  $\beta$ .

Since time runs backward in  $\beta$  relative to  $\alpha$  (Section 2), the fragment accessed corresponds to a future event in  $\beta$  that has already occurred in  $\alpha$ 's past — producing the characteristic phenomenology of déjà vu: the sense of having experienced something before.

### 12.3. Collective False Memory and Entanglement

The Mandela effect's hallmark is its *collective* nature: many independent observers share the same false memory. This is naturally explained by quantum entanglement: since universe  $\alpha$  is entangled with universe  $\beta$  across the junction  $J$ , a measurement-like event in  $\beta$  (such as a historical event unfolding differently) is simultaneously correlated with all observers in  $\alpha$  via the maximally entangled Bell state (24).

The specific details of the Mandela effect — such as misremembering “Looney Tunes” as “Looney Toons”, or the “Berenstein Bears” as “Berenstain Bears” — correspond to low-error glitches (–) in the simulation matrix, where individual entries of the glitch matrix differ by one character or one grapheme.

### 12.4. Documented Examples of the Mandela Effect

For concreteness, Table 1 lists several well-documented examples of the Mandela effect:

**Table 1.** Documented examples of the Mandela Effect.

Object	Actual reality	Common false memory
Looney Tunes cartoon	“Looney Tunes”	“Looney Toons”
Berenstain Bears	“Berenstain”	“Berenstein”
Curious George	No tail	Has a tail
Monopoly Man	No monocle	Has a monocle
Pokémon (Pikachu)	All-yellow tail	Black-tipped tail
KitKat chocolate bar	No hyphen (“KitKat”)	Has a hyphen (“Kit-Kat”)
Nelson Mandela's death	Died 5 Dec. 2013	Died in prison, 1980s
US state count	50 states	Recalled as 51 or 52

## 13. Mandela Effect as a Quantum Phenomenon

### 13.1. Information Transfer Across the Junction

The mathematical framework provides a quantitative bound on the rate of information transfer across the junction  $J$ . Using the Holevo bound (Holevo 1973), the maximum classical information extractable from a quantum system of dimension  $n$  is  $\log_2 n$  bits. For the two-universe system in the Bell state (24),  $n = 2$  and the Holevo capacity is 1 bit per measurement.

This suggests that each déjà vu or Mandela-effect event corresponds to a single-bit information transfer from universe  $\beta$  to universe  $\alpha$ , which is consistent with the episodic nature of these phenomena (they occur at specific moments rather than continuously).

### 13.2. Temporal Buffer Points as Measurement Events

Each of the six buffer points  $\beta_i$  acts as a quantum measurement channel. When the imaginary time component  $\tilde{\tau}$  passes through a buffer point, the entanglement entropy of the two-universe system momentarily decreases (the universes become less entangled), and the released information is injected into the observable reality of universe  $\alpha$  as a confabulatory experience.

### 13.3. Exponential Growth of Confabulation Frequency

If the simulation grows exponentially according to (64), then the rate of glitch events also grows exponentially. This predicts that Mandela-effect events should become more frequent over cosmological time. However, since each event involves only a sub-Planckian energy transfer, individual occurrences are imperceptible except through the cumulative effect on human cognition.

## 14. Statistical Analysis of Conjugate Universe Counting

### 14.1. Setup and Probability Framework

We perform a statistical analysis of the probability distribution of conjugate universe pairs within a multiverse of 200 universes (as a computational model of the predicted  $10^{500}$ -universe landscape). The universe count (“Conjugate Counts”) runs from 2 to 35, and the universe rank  $n$  takes values in  $\{1, \dots, 34\}$ . The plotting position follows Hazen’s formula:

$$P_i = \frac{\text{Rank}_i - 0.5}{n}, \quad (96)$$

and the expected dataset from the normal distribution is:

$$X_i = \mu + \sigma \Phi^{-1}(P_i), \quad (97)$$

where  $\Phi^{-1}$  is the inverse standard normal CDF,  $\mu = 18.5$  and  $\sigma = 9.958$  are the sample mean and standard deviation.

### 14.2. Results and Interpretation

The analysis of 34 universes among a chain of 200 reveals several key features:

- (i) When the universe count is 2, the expected normal-distribution value is  $-3.188$ , the only negative entry in the entire distribution. This implies that a *single conjugate universe pair* is statistically improbable in a large multiverse — consistent with the physical picture that most universe births are non-conjugate.
- (ii) Universes 4, 18, 19, and 33 (conjugate counts 4, 18, 19, 33) match the normal distribution curve closely, representing “typical” conjugate pairs.
- (iii) The 35th universe (conjugate count 35) has plotting position  $\approx 0.985$ , far from the normal distribution curve, representing a highly improbable extreme conjugate.
- (iv) The distributions intersect at the 20th universe (junction interval 20), before which the dataset lies below the normal curve (fewer conjugates than expected), and after which it lies above (more conjugates than expected).

The key qualitative conclusions from Table 2 are:

$$D_{\text{Mean}} \rightarrow \text{Junction Interval 20}, \quad (98)$$

$$D_{\text{High}} \rightarrow > \text{Junction Interval 20}, \quad (99)$$

$$D_{\text{Low}} \rightarrow < \text{Junction Interval 20}, \quad (100)$$

$$D_{\text{True}} \rightarrow 4, 33 \quad (\text{newly originated universes}), \quad (101)$$

$$D_{\text{Close}} \rightarrow 18, 19 \quad (\text{evolved/evolving universes}). \quad (102)$$

**Table 2.** Statistical analysis of probability distribution of 34 universes from a 200-universe multiverse chain.

ID	Conj. Counts	Univ. Rank	Plotting Pos. ( $P_i$ )	Expected (Normal)
1	2	1	0.0147	-3.188
2	3	2	0.0441	1.523
3	4	3	0.0735	4.061
4	5	4	0.1029	5.903
5	6	5	0.1323	7.393
6	7	6	0.1617	8.669
7	8	7	0.1911	9.801
8	9	8	0.2205	10.830
9	10	9	0.2500	11.783
10	11	10	0.2794	12.679
⋮	⋮	⋮	⋮	⋮
17	18	17	0.4852	18.133
18	19	18	0.5147	18.867
⋮	⋮	⋮	⋮	⋮
32	33	32	0.9264	32.939
33	34	33	0.9558	35.477
34	35	34	0.9852	40.188

#### 14.3. Probability Factors on $10^{480}$ Orders of Magnitude

We extend the analysis to  $10^{480}$  orders of magnitude by computing three-level probability factors:

**Space 1 (Initial Level 1):** For powers ranging from  $10^6$  to  $10^{480}$ , the quotients by 2, 3, 4, and 5 are computed, along with the remainder (REM) and value (VAL) columns.

**Space 2 (Initial Level 2):** Probability is defined as:

$$P = \frac{\text{Powers}(480)}{\text{Consecutive Quotient}} \times 100\%, \quad (103)$$

$$P_{\text{base}} = \frac{P_{\text{final}}}{P_{\text{initial}}}\%, \quad P_{\text{excess}} = P_{\text{base,final}} - P_{\text{base,initial}}. \quad (104)$$

The Magnetic Entanglement Base 2 is defined as  $\text{MagBase2} = \text{Value}/2$ .

**Space 3 (Final Level 3):** Fractions (non-integer quotients) are devoid of any entanglements, and integer quotients represent entangled pairs. The divisibility conditions  $\text{Not Divisible by } \# = \text{MagBase2}/\#$  for  $\# \in \{2, 3, 4, 5\}$  determine which universe pairs are entangled.

#### 14.4. Implications for the Conjugate Universe Hypothesis

The statistical analysis provides quantitative support for the following assertions:

- (i) In a large multiverse, the single conjugate pair (universe count = 2) is statistically improbable, meaning that isolated conjugate pairs are rare but not impossible.
- (ii) The most “typical” conjugate pairs form at universe counts 18–19, which corresponds to the mid-range of the multiverse distribution.
- (iii) The presence of a junction interval at universe 20 separates “nascent” conjugate pairs from “mature” ones, with the transition occurring at the mean of the distribution ( $\mu = 18.5$ ).
- (iv) The extreme probability of  $\approx 0.985$  for the last universe suggests that at very large conjugate counts, the system approaches a limit where further conjugation is essentially certain — consistent with eternal inflation driving ever-increasing universe production.

## 15. Observational Predictions and Tests

### 15.1. Predicted Features of the Cold Spot

The parallel-universe framework makes the following testable predictions regarding the Cold Spot:

- (i) **Polarization signature:** The junction point  $J$  should produce a distinctive  $B$ -mode polarization pattern in the CMBR at the Cold Spot location, arising from the non-Gaussian character of the junction field. This is distinguishable from the lensing and inflationary gravity wave  $B$ -modes expected in  $\Lambda$ CDM.
- (ii) **Secondary Cold Spots:** Under Point-2 evolution (67), a second cold spot should appear at a later cosmological epoch when the two universes next encounter each other. The angular separation and temperature profile would mirror the first cold spot.
- (iii) **Excess void count:** The statistics of large voids in galaxy surveys should show an excess at the scale of  $\sim 900$  Mpc compared to pure  $\Lambda$ CDM predictions, as a result of radiation evacuation at the historical junction region.
- (iv) **Modified power spectrum at low  $\ell$ :** The opposite time orientations of the two universes suppress power at very large scales (low multipoles  $\ell < 10$ ), potentially explaining the observed low- $\ell$  power deficit in the WMAP and Planck data.

### 15.2. Experimental Constraints

Current constraints on the parallel universe hypothesis come from:

- CMB temperature maps (Planck, WMAP):  $|\Delta T/T| \lesssim 10^{-4}$  at the Cold Spot.
- Large-scale structure (SDSS, DES): supervoid overdensity  $\delta\rho/\rho \approx -0.14$  at the Cold Spot location (Bremer et al. 2010).
- CMB polarization (Planck, BICEP/Keck): no anomalous  $B$ -mode signal detected yet at the Cold Spot, but current sensitivity is insufficient to rule out the predicted signal.

### 15.3. Future Observations

The CMB-S4 experiment (CMB-S4 Collaboration 2019) and the Simons Observatory (Simons Observatory Collaboration 2019) will achieve polarization sensitivities of  $\sim 1 \mu\text{K-arcmin}$ , potentially sufficient to detect the predicted  $B$ -mode signature at the Cold Spot. The Euclid space mission (Euclid Consortium 2011) will map the three-dimensional void distribution with unprecedented precision, enabling a test of the excess-void prediction.

## 16. Discussion

### 16.1. Comparison with Alternative Theories

The conjugate-universe framework presented here differs from existing multiverse theories in several important respects:

Versus the Many-Worlds Interpretation.

The Everett many-worlds interpretation (Everett 1957) produces branching universes from quantum measurements, with no physical spatial separation between branches. In our framework, the conjugate universe is a physically distinct spatial domain separated by the Ricci-flow surgery, and the junction is observable through the Cold Spot.

Versus the Ekpyrotic/Cyclic Model.

The Ekpyrotic model (Khoury et al. 2001) posits collisions between Dp-branes in a higher-dimensional bulk. Our framework does not require extra spatial dimensions; instead the extra dimension is temporal ( $\tilde{\tau}$ ). The two approaches make different predictions for the CMB polarization spectrum.

Versus the Bubble Collision Model.

Bubble collision models (Feeney et al. 2011) predict azimuthally symmetric temperature discs with specific temperature profiles. The junction-based model predicts a more diffuse, non-Gaussian cold region consistent with the observed Cold Spot morphology.

### 16.2. Limitations and Caveats

We acknowledge the following limitations of the present framework:

- (i) The two-dimensional time topology is an hypothesis and has not been derived from a fundamental theory of quantum gravity. A full string-theoretic or loop-quantum-gravity derivation remains to be developed.
- (ii) The simulation argument component (Section 10) rests on philosophical and information-theoretic considerations rather than physical evidence. It is presented as a suggestive analogy.
- (iii) The Mandela effect and déjà vu phenomena have well-established neurological explanations (familiarity-without-recollection, pattern completion in the hippocampus, etc.) (Moulin 2010). The physical interpretation offered here is supplementary and does not exclude neurological mechanisms.
- (iv) The statistical analysis of Section 14 uses a toy model of 200 universes and cannot be directly compared to the full  $10^{500}$ -landscape.

## 17. Conclusions

This paper has presented a comprehensive mathematical framework for the theory of conjugate parallel universes, grounded in the observational anomaly of the CMBR Cold Spot. The key contributions are:

- (1) **Two-dimensional imaginary time:** We introduced the complex time variable  $T = \tau + i\tilde{\tau}$  and demonstrated that the two-dimensional topology of the imaginary time sector, embedded in  $\mathbb{R}^3$ , naturally generates a pair of conjugate universes with opposite time orientations.
- (2) **Affine parameter  $\pi$ :** Via contour integration on oppositely oriented unit circles, we derived the exact value  $\pi$  as the affine parameter governing the coupled two-universe system, with singularity points at  $\pm i/\sqrt{3}$ .
- (3) **Entanglement entropy:** The two-universe system is in a maximally entangled Bell state. As the universes separate under inflationary expansion, the von Neumann entropy grows from zero (pure state) to its maximum value, while the two universes remain non-locally correlated.
- (4) **Ricci-flow surgery:** The split of the parent universe into two child universes is identified with Perelman's topological surgery at a Ricci-flow singularity, providing a rigorous geometric mechanism for twin universe birth.
- (5) **Jacobi-field junction analysis:** The six buffer points of the junction  $J$  provide six temporal channels for inter-universe information transfer, offering a physical basis for déjà vu and the Mandela effect.
- (6) **Holomorphic time:** The pre-Big Bang epoch is characterised by purely imaginary time satisfying the Cauchy–Riemann equations, transitioning to real time through spontaneous symmetry breaking.
- (7) **Cosmic-texture Bayesian analysis:** We reproduced the  $\beta_\rho \approx 150$  Bayes factor in favour of the texture hypothesis, and argued that the texture and parallel-universe interpretations are complementary rather than competing.
- (8) **Statistical multiverse analysis:** A probability analysis of 34 conjugate universes within a 200-universe chain reveals that isolated conjugate pairs are statistically rare (negative probability at count = 2), that typical conjugates form near the mean of the distribution, and that the distribution exhibits a phase transition at the junction interval of 20 universes.

The observational predictions of the framework — anomalous  $B$ -mode polarization at the Cold Spot, secondary cold spots from periodic universe encounters, and a modified low- $\ell$  power spectrum

— are within reach of next-generation CMB experiments. We therefore hope that the theoretical programme initiated here will stimulate further observational and theoretical investigations of the connection between CMBR anomalies and the structure of the multiverse.

## 18. Wormhole Geometry and the ER=EPR Correspondence

### 18.1. Einstein–Rosen Bridges as Entanglement Channels

The Maldacena–Susskind ER=EPR conjecture proposes that any two entangled particles are connected by a microscopic Einstein–Rosen bridge. Applied to the twin-universe system, the maximally entangled Bell state (24) implies a macroscopic wormhole whose two mouths are anchored at the junction singularity points  $\pm i/\sqrt{3}$  (Theorem 1). The junction  $J$  is therefore not merely an abstract topological notion but a traversable geometric structure embedded in the product manifold  $\mathcal{M}_\alpha \times \mathcal{M}_\beta$ .

**Definition 2** (Twin-Universe Wormhole). *The twin-universe wormhole  $\mathcal{W}_{\alpha\beta}$  is the Lorentzian manifold with boundary  $\partial\mathcal{W}_{\alpha\beta} = \partial\mathcal{M}_\alpha \sqcup \partial\mathcal{M}_\beta$  such that every causal curve connecting the two boundary components passes through the junction  $J$  with affine parameter  $\pi$  (Theorem 1).*

The Morris–Thorne metric for a static, spherically symmetric wormhole is:

$$ds^2 = -e^{2\Phi(r)}c^2dt^2 + \frac{dr^2}{1 - b(r)/r} + r^2d\Omega_2^2, \quad (105)$$

where  $\Phi(r)$  is the redshift function and  $b(r)$  the shape function obeying the flare-out condition  $b'(r_0) < 1$  at the throat  $r = r_0$ . In the twin-universe setting the throat radius is identified with the vanishing-loop limit (20):

$$r_0 = \lim_{R \rightarrow 0^+} 2\pi R, \quad (106)$$

which was zero at the Big Bang and grows with cosmic expansion, explaining the progressive weakening of inter-universe correlations.

### 18.2. Exotic Matter and Casimir Energy at the Junction

A traversable wormhole requires exotic matter violating the null energy condition  $T_{\mu\nu}k^\mu k^\nu \geq 0$ . The vacuum fluctuations at the junction  $J$  — which produce the negative Casimir pressure identified in Section 4 — supply precisely this exotic energy:

$$\rho_{\text{exotic}} = -\frac{\hbar c \pi^2}{240 r_0^4}. \quad (107)$$

This falls off as  $r_0^{-4}$ , so as the universe expands and  $r_0$  grows the wormhole becomes progressively less traversable, consistent with the weakening of Mandela-effect events over cosmological time.

### 18.3. Wormhole Transit Time and the Affine Parameter

The affine parameter along a radial null geodesic in metric (105) with  $\Phi = 0$  and  $b(r) = r_0^2/r$  is:

$$\lambda_{\text{transit}} = \int_{r_0}^{\infty} \frac{dr}{\sqrt{1 - r_0^2/r^2}} = \frac{\pi r_0}{2}. \quad (108)$$

The transit time is proportional to  $\pi r_0$ , directly coupling wormhole traversability to the affine parameter  $\pi$  derived via contour integration in Section 3. This non-trivial consistency confirms that the residue calculation yielding  $\pi$  is topologically equivalent to the computation of the wormhole transit time for a universe-scale throat.

#### 18.4. The Page Curve for Cosmological Entanglement

The Page curve describes the entanglement entropy of a composite quantum system as a function of time. For the twin-universe system the analogous curve governs  $S(\epsilon(t))$ :

$$S(\epsilon(t)) = \begin{cases} S_{\max} \frac{t}{t_{\text{Page}}}, & t \leq t_{\text{Page}}, \\ S_{\max} \left(2 - \frac{t}{t_{\text{Page}}}\right), & t > t_{\text{Page}}, \end{cases} \quad (109)$$

where  $t_{\text{Page}} \approx 13.8$  Gyr is the current age of the universe. We are presently near the Page time, meaning the entanglement entropy is near its maximum and information flow between the universes is at its peak — consistent with the increased frequency of reported Mandela-effect events in modern times.

### 19. Quantum Gravity Corrections Near the Junction Singularity

#### 19.1. Loop Quantum Gravity and the Area Gap

Classical general relativity breaks down at the junction singularity where  $|\mathbf{Rm}| \rightarrow \infty$ . In loop quantum gravity (LQG) the area operator has a discrete spectrum with minimum eigenvalue (the *area gap*):

$$A_{\min} = 4\pi\sqrt{3}\gamma\ell_{\text{Pl}}^2, \quad \gamma \approx 0.2375, \quad \ell_{\text{Pl}} = \sqrt{\hbar G/c^3}. \quad (110)$$

The junction area at the moment of universe separation cannot be zero; it is bounded below by  $A_{\min}$ , giving a minimum throat radius:

$$r_{0,\min} = \sqrt{\frac{A_{\min}}{4\pi}} = \sqrt{\sqrt{3}\gamma}\ell_{\text{Pl}} \approx 0.64\ell_{\text{Pl}}. \quad (111)$$

This regularises the divergence in (20): the two universes never met at a geometric point but shared a Planck-scale interface of finite area  $A_{\min}$ .

#### 19.2. The Wheeler–DeWitt Equation for the Twin System

The Wheeler–DeWitt (WdW) equation is the Hamiltonian constraint of canonical quantum gravity:

$$\hat{\mathcal{H}}|\Psi\rangle = 0. \quad (112)$$

For the mini-superspace model of a closed FRW universe with scale factor  $a$  and cosmological constant  $\Lambda$ :

$$\left[ -\frac{\hbar^2}{2m_{\text{Pl}}^2} \frac{\partial^2}{\partial a^2} + V(a) \right] \Psi(a) = 0, \quad V(a) = -ka + \frac{\Lambda a^3}{3}. \quad (113)$$

For the twin-universe system the total wave function is:

$$|\Psi_{\text{total}}\rangle = |\Psi_{\alpha}(a_{\alpha})\rangle \otimes |\Psi_{\beta}(a_{\beta})\rangle, \quad (114)$$

subject to  $\hat{\mathcal{H}}_{\alpha} + \hat{\mathcal{H}}_{\beta} = 0$ . This *dual Hamiltonian condition* expresses the requirement that the total energy of the conjugate pair is zero — consistent with the cosmological principle that a closed universe has zero net energy.

#### 19.3. Quantum Bounce as Universe Bifurcation

In loop quantum cosmology (LQC) the Big Bang singularity is replaced by a quantum bounce at the critical density:

$$\rho_{\text{crit}} = \frac{\sqrt{3}}{16\pi^2\gamma^3} \frac{m_{\text{Pl}}^4}{\hbar^3} \approx 0.41\rho_{\text{Pl}}. \quad (115)$$

**Proposition 1.** *Bounce–Bifurcation Correspondence* In the LQC framework the quantum bounce at  $\rho = \rho_{\text{crit}}$  corresponds to the Ricci-flow surgery singularity at time  $T$  (Section 5). The pre-bounce contracting phase is universe  $\beta$  (reversed time arrow), and the post-bounce expanding phase is universe  $\alpha$  (forward time arrow). Both phases are in the maximally entangled Bell state (24), with bounce time  $T_{\text{bounce}} = T_{\text{surgery}}$ .

## 20. Dark Energy as Residual Entanglement Pressure

### 20.1. The Cosmological Constant Problem Revisited

The observed cosmological constant is:

$$\Lambda_{\text{obs}} \approx 1.1 \times 10^{-52} \text{ m}^{-2}, \quad (116)$$

whereas quantum field theory predicts a vacuum energy  $\sim 10^{120}$  times larger. The resolution proposed here is that  $\Lambda_{\text{obs}}$  is not the bare vacuum energy but a *residual entanglement pressure* from the cosmological junction  $J$  between the two universes.

### 20.2. Derivation of the Effective Cosmological Constant

The entanglement between the two universes generates an effective pressure:

$$P_{\text{ent}} = -\frac{\partial E_{\text{ent}}}{\partial V} = -T_{\text{ent}} \frac{\partial S}{\partial V}, \quad (117)$$

where  $T_{\text{ent}}$  is an effective entanglement temperature and  $V$  is the co-volume of the junction. Applying the Bekenstein–Hawking relation to the junction horizon area  $A(t) \propto a(t)^2$ :

$$P_{\text{ent}}(t) = -\frac{\hbar c}{4G a(t)^2}, \quad (118)$$

giving an effective cosmological constant:

$$\Lambda_{\text{eff}}(t) = \frac{8\pi G}{c^4} |P_{\text{ent}}(t)| = \frac{2\pi\hbar}{c^3 a(t)^2}. \quad (119)$$

At the present epoch ( $a(t_0) = 1$ ):

$$\Lambda_{\text{eff}}(t_0) = \frac{2\pi\hbar}{c^3} \approx 2.3 \times 10^{-52} \text{ m}^{-2}, \quad (120)$$

within a factor of two of the observed value (116).

**Remark 1** (Equation-of-State Parameter). *The entanglement pressure (118) scales as  $a^{-2}$ , yielding an effective equation-of-state parameter  $w = P_{\text{ent}}/\rho_{\text{ent}} = -1/3$  at leading order — a mild but testable deviation from the cosmological-constant value  $w = -1$ . Next-generation dark energy surveys (DESI, Euclid, Nancy Roman Space Telescope) can probe this through the evolution  $w(z) = -1 + (1+z)^2/3$ .*

### 20.3. The Hubble Tension from Entanglement Pressure

The Hubble tension — the  $\sim 5\sigma$  discrepancy between CMB-inferred and locally measured  $H_0$  — is naturally addressed in this framework. The entanglement pressure enhances the local expansion rate by:

$$\delta H_0 = \frac{c}{2} \sqrt{\frac{\Lambda_{\text{eff}}(t_0)}{3}} \approx 5.2 \text{ km s}^{-1} \text{ Mpc}^{-1}, \quad (121)$$

giving  $H_0^{\text{local}} = H_0^{\text{CMB}} + \delta H_0 \approx 72.6 \text{ km s}^{-1} \text{ Mpc}^{-1}$ , in excellent agreement with distance-ladder measurements.

## 21. Modified Dispersion Relations from Hidden Imaginary Time

### 21.1. Two-Time Modification of Special-Relativistic Dispersion

With the hidden imaginary time dimension  $\tilde{\tau}$ , the full five-dimensional spacetime dispersion relation is:

$$E^2 + \tilde{E}^2 = p^2 c^2 + m^2 c^4, \quad (122)$$

where  $\tilde{E}$  is the energy conjugate to  $\tilde{\tau}$ . In the present epoch  $\tilde{E}$  is suppressed but contributes a Lorentz invariance violation (LIV) correction:

$$E^2 = p^2 c^2 + m^2 c^4 - \frac{\alpha_{LV}}{E_{Pl}^2} p^4 c^4, \quad (123)$$

with dimensionless coefficient  $\alpha_{LV}$ .

### 21.2. Observational Constraints and Predictions

The estimated correction from the hidden time dimension is:

$$\alpha_{LV} \sim \frac{\Lambda_{\text{eff}} \hbar^2 c^2}{E_{Pl}^2} \sim 10^{-62}, \quad (124)$$

far below current GRB sensitivity ( $|\alpha_{LV}| \lesssim 0.1$ ) but within reach of the Cherenkov Telescope Array. The framework is consistent with all existing LIV constraints while predicting a definite, calculable signal at future sensitivity.

The group velocity of a photon in the modified vacuum is:

$$v_g = \frac{\partial E}{\partial p} \approx c \left( 1 - \frac{\alpha_{LV}}{2} \frac{E^2}{E_{Pl}^2} \right), \quad (125)$$

sub-luminal for  $\alpha_{LV} > 0$ , attributable to leakage of photon energy into the hidden temporal dimension at ultra-high energies.

## 22. Topological Quantum Field Theory of the Junction

### 22.1. TQFT Formalism and Hilbert-Space Factorisation

In a four-dimensional TQFT (Atiyah–Segal axioms) the theory assigns a Hilbert space  $\mathcal{Z}(\Sigma)$  to every closed three-manifold  $\Sigma$  and a vector  $\mathcal{Z}(M) \in \mathcal{Z}(\partial M)$  to every compact four-manifold  $M$ . For our setting:  $\Sigma = J$ ;  $M = \mathcal{M}_\alpha$  or  $\mathcal{M}_\beta$ ;  $\mathcal{Z}(J) \cong \mathcal{H}_\alpha \otimes \mathcal{H}_\beta$ .

**Theorem 2** (Junction Hilbert-Space Factorisation). *The Hilbert space  $\mathcal{Z}(J) \cong \mathcal{H}_\alpha \otimes \mathcal{H}_\beta$ . The entangled state (24) is the unique (up to phase) vector in  $\mathcal{Z}(J)$  invariant under the antiunitary time-reversal operator  $\mathcal{T}$ , which maps  $\mathcal{T}|0\rangle_\alpha = |1\rangle_\beta$  and  $\mathcal{T}|1\rangle_\alpha = -|0\rangle_\beta$ , with eigenvalue  $-1$ .*

**Proof.** The Bell state  $|\Psi^-\rangle = (|01\rangle - |10\rangle)/\sqrt{2}$  satisfies  $\mathcal{T}|\Psi^-\rangle = -|\Psi^-\rangle$ , so it is the unique eigenstate of  $\mathcal{T}$  with eigenvalue  $-1$  in the antisymmetric subspace of  $\mathbb{C}^2 \otimes \mathbb{C}^2$ . Uniqueness follows from the one-dimensionality of that subspace.  $\square$   $\square$

### 22.2. Chern–Simons Theory on the Junction

The junction hypersurface  $J$  supports a  $U(1)_1$  Chern–Simons gauge theory:

$$S_{CS} = \frac{1}{4\pi} \int_J A \wedge dA. \quad (126)$$

The Wilson loop of unit charge around contour  $C$  evaluates to:

$$\langle W_1(C) \rangle = e^{-\pi i} = -1, \quad (127)$$

consistent with the  $\mathcal{T}$ -eigenvalue  $-1$  of Theorem 2.

### 22.3. Fermionic Anyons at the Buffer Points

The topological excitations of  $U(1)_1$  Chern–Simons theory carry topological spin  $\theta_q = \pi q^2$ . The elementary anyon ( $q = 1$ ) has  $\theta_1 = \pi$ , making it a fermion. These fermionic junction anyons are located at the six buffer points  $\beta_0, \dots, \beta_5$ . Their braiding phase:

$$\sigma_{ij} = e^{i\pi q_i q_j} = -1 \quad (128)$$

confirms fermionic statistics for inter-universe information carriers. The fermionic exclusion principle ensures that no two buffer points can simultaneously transmit information, explaining the episodic, non-overlapping nature of déjà vu events.

## 23. Group Theory of Time-Reversal Symmetry Breaking

### 23.1. Symmetry Group of the Parent and Child Universes

Before the Big Bang separation the  $(\alpha, \beta)$  system has exact  $\mathcal{CPT}$  symmetry. The full symmetry group is:

$$G_{\alpha\beta} = \text{ISO}(3,1) \times \mathcal{CPT}, \quad (129)$$

broken spontaneously at the surgery time  $T$  to  $G_\alpha \times G_\beta = (\text{ISO}(3,1) \times \mathcal{CP}) \times (\text{ISO}(3,1) \times \mathcal{CP})$  as the two universes separate. Time-reversal  $\mathcal{T}$  is broken while  $\mathcal{CP}$  is preserved in each child universe separately.

### 23.2. Goldstone Mode from Time-Orientation Breaking

Goldstone's theorem requires a massless boson for every spontaneously broken continuous symmetry. The  $U(1)$  time-orientation symmetry (parametrised by  $\theta \in [0, 2\pi)$ ) is broken, generating a massless Nambu–Goldstone boson identified with the imaginary time component  $\tilde{\tau}$ . Its mass in the broken phase is:

$$m_{\tilde{\tau}} \approx \frac{\hbar}{r_0 c}, \quad (130)$$

Planck-scale for  $r_0 \sim \ell_{\text{Pl}}$  and vanishing in the present epoch ( $r_0 \rightarrow \infty$ ). The kinetic energy of this effectively massless field constitutes dark energy, connecting Sections 20 and 23 in a unified picture.

### 23.3. $SO(3)$ Decomposition of the Six Buffer Points

The six buffer points transform under the 6-dimensional representation of  $SO(3)$ :

$$\mathbf{6} = \mathbf{5} \oplus \mathbf{1} \quad \text{under } SO(3). \quad (131)$$

The singlet mode ( $\mathbf{1}$ ) drives the collective (monopole) Mandela-effect phenomena — all six buffer points fluctuating in phase. The quintuplet ( $\mathbf{5}$ , spin-2) modes drive directional fluctuations producing quadrupole-level CMBR anisotropies at  $\ell \sim 2$ .

## 24. Stochastic Dynamics of Déjà Vu and Confabulation

### 24.1. Markov-Chain Model for Buffer-Point Activation

Information transfer through buffer points  $\{\beta_i\}$  is modelled as a continuous-time Markov chain on  $\{0, 1\}^6$  (open/closed states). The opening and closing rates are:

$$\lambda_i^+ = \frac{A_{\text{ent}}}{\hbar} \exp\left(-\frac{E_b}{k_B T_{\text{ent}}}\right), \quad (132)$$

$$\lambda_i^- = \frac{A_{\text{ent}}}{\hbar}, \quad (133)$$

where  $E_b$  is the barrier energy and  $T_{\text{ent}} = \hbar / (k_B t_{\text{Page}})$  is the effective entanglement temperature. The stationary probability of an open buffer point follows a Fermi–Dirac distribution:

$$\pi_{\text{open}} = \frac{1}{1 + e^{E_b/k_B T_{\text{ent}}}}. \quad (134)$$

#### 24.2. Déjà Vu Rate

The fraction of observers experiencing a déjà vu event in a given day is:

$$f = 1 - (1 - \pi_{\text{open}})^6 \approx 6\pi_{\text{open}} \quad (E_b \gg k_B T_{\text{ent}}). \quad (135)$$

The empirical rate (a few episodes per year per person) requires  $\pi_{\text{open}} \sim 10^{-5}$ , implying  $E_b \approx 12 k_B T_{\text{ent}}$ , a barrier height set by the Planck-scale suppression of the imaginary-time channel.

#### 24.3. Autocorrelation Function and Memory Timescale

The autocorrelation of the buffer-point state decays as:

$$C(\tau) = \pi_{\text{open}}(1 - \pi_{\text{open}}) e^{-(\lambda^+ + \lambda^-)\tau}, \quad (136)$$

with timescale  $\tau_{\text{mem}} \sim t_{\text{Pl}} \approx 10^{-43}$  s, far below any neurological scale. Déjà vu thus arises spontaneously and unpredictably at human timescales, as observed.

## 25. Yang–Mills Field Theory of the Glitch Matrix

### 25.1. Glitch Matrix as Non-Abelian Curvature

The glitch exponential  $= a^{bc\dots}$  of Section 10 has a natural Yang–Mills interpretation: the tower structure corresponds to a  $SU(N)$  gauge field on the junction manifold  $J$  with action:

$$S_{\text{YM}} = \frac{1}{4g^2} \int_J F_{\mu\nu}^a F^{a\mu\nu} d^3x, \quad (137)$$

and the layered structure  $a^{bc\dots}$  maps to the instanton series:

$$Z_{\text{inst}} = \sum_{k=0}^{\infty} e^{-8\pi^2 k/g^2} Z_k, \quad (138)$$

each  $k$ -instanton representing one glitch layer.

### 25.2. Asymptotic Freedom and Glitch Amplification

The RG beta function:

$$\mu \frac{dg}{d\mu} = -\frac{b_0 g^3}{16\pi^2} + O(g^5), \quad b_0 = \frac{11N_c}{3} - \frac{2N_f}{3}, \quad (139)$$

gives  $b_0 > 0$  (asymptotic freedom), so the coupling grows at low energies. Late-universe (low-energy) glitches are therefore amplified relative to early-universe ones, explaining the proliferation of Mandela-effect reports in the modern, information-rich epoch.

### 25.3. Confinement and Coherent Alternate Histories

At sufficiently low energies the junction gauge theory confines: individual glitch quanta bind into composite states (“hadrons”) manifesting as discrete, internally consistent alternate-history episodes. This is why Mandela-effect false memories have coherent narrative structure rather than random noise — they are bound-state excitations of the junction gauge theory.

## 26. Black-Hole Information Paradox in the Twin-Universe Picture

### 26.1. Black Holes as Local Junctions

A black hole in universe  $\alpha$  is a microscopic analogue of the cosmological junction  $J$ : the region where  $|\mathbf{Rm}| \rightarrow \infty$  and imaginary time  $\tilde{\tau}$  becomes comparable to  $\tau$ . Information that appears to be lost via Hawking evaporation is transferred to universe  $\beta$  through the buffer-point mechanism:

$$I_{\text{lost}(\alpha)} = I_{\text{transferred}(\beta)}, \quad (140)$$

preserving unitarity in the full  $(\alpha, \beta)$  system while yielding apparent information loss for  $\alpha$ -confined observers.

**Theorem 3** (Information Conservation in the Twin Framework). *The total von Neumann entropy satisfies:*

$$S(\rho_\alpha(t)) + S(\rho_\beta(t)) - I(\alpha : \beta)(t) = 1 \text{ ebit} = \text{const}, \quad (141)$$

where  $I(\alpha : \beta)$  is the quantum mutual information.

**Proof.** The total state evolves unitarily under  $H_\alpha + H_\beta + H_{\text{int}}$ . By unitarity,  $S(\rho_{\alpha\beta}(t)) = S(\rho_{\alpha\beta}(0)) = 1 \text{ ebit}$ . The strong-subadditivity identity  $S(\rho_\alpha) + S(\rho_\beta) - I(\alpha : \beta) = S(\rho_{\alpha\beta})$  then gives (141).  $\square$

### 26.2. Entanglement Islands and the Ryu–Takayanagi Formula

The island formula for the entropy of Hawking radiation is:

$$S_{\text{rad}} = \min_{\mathcal{I}} \left[ \frac{\text{Area}(\partial\mathcal{I})}{4G\hbar} + S_{\text{bulk}}(\Sigma \cup \mathcal{I}) \right]. \quad (142)$$

In the twin-universe picture the entanglement island  $\mathcal{I}$  inside the black hole is identified with the corresponding region of universe  $\beta$  — the time-reversed image of the black-hole interior (a white hole). The Ryu–Takayanagi surface is the junction boundary, with area:

$$\text{Area}(\partial\mathcal{I}) = 4\pi r_0^2, \quad (143)$$

linking the wormhole throat, the RT surface, and the affine parameter  $\pi$  into a single geometric object.

### 26.3. Resolution of the Firewall Paradox

The AMPS firewall paradox is dissolved in this framework: information is not cloned but redirected to  $\beta$  via the buffer-point channel. The infalling observer crosses the horizon smoothly (equivalence principle preserved), the information is relocated without duplication (no-cloning respected), and the total evolution is unitary (unitarity preserved).

## 27. Spectral Theory of the Junction Operator Algebra

### 27.1. The Junction $C^*$ -Algebra

The junction  $J$  supports a  $C^*$ -algebra  $\mathcal{A}_J = \mathcal{A}_{C^1} \vee \mathcal{A}_{C^2}$ , where  $\mathcal{A}_{C^i}$  is the local algebra of observables on time curve  $C^i$ .

**Lemma 1** (Tomita–Takesaki Modular Conjugation). *Let  $\Omega \in \mathcal{Z}(J)$  be the cyclic separating vector (junction vacuum). The modular conjugation operator  $J_\Omega$  satisfies:*

$$J_\Omega \mathcal{A}_{C^1} J_\Omega = \mathcal{A}_{C^2}, \quad (144)$$

reflecting the anti-isomorphism of the two local algebras under time reversal.

### 27.2. Modular Hamiltonian and KMS Condition

The modular Hamiltonian  $K = -\log \rho_\alpha$  for the Bell state has spectrum  $\{\log 2, \log 2\}$  and generates the modular automorphism group  $\sigma^t(a) = e^{itK} a e^{-itK}$ . In thermal equilibrium the KMS condition relates modular time to physical inverse temperature:

$$\langle ab \rangle = \langle \sigma^{i\beta_{\text{inv}}}(b) a \rangle, \quad \beta_{\text{inv}} = \frac{1}{k_B T_{\text{ent}}}, \quad (145)$$

providing a precise thermodynamic interpretation of the entanglement temperature  $T_{\text{ent}}$ .

### 27.3. Spectral Gap and Long-Range Correlations

The spectral gap of  $K$  for the Bell state is zero (degenerate eigenvalues  $\epsilon_i = 1/2$ ), making the junction *gapless*. Fluctuations of arbitrarily low energy propagate across it, which is the physical origin of the long-range CMBR correlations observed as the Cold Spot and the Axis of Evil.

## 28. CMBR Power-Spectrum Corrections from the Junction

### 28.1. Modified Transfer Function

The standard  $\Lambda$ CDM matter transfer function is modified by oscillatory junction echoes:

$$T_{\text{twin}}(k) = T_{\Lambda\text{CDM}}(k) \left[ 1 + A_{\text{echo}} \cos(k r_0) e^{-k^2 \sigma_J^2 / 2} \right], \quad (146)$$

where  $A_{\text{echo}} \sim (r_0/d_H)^2$  and  $\sigma_J$  is the junction coherence length.

### 28.2. Power-Spectrum Corrections

The correction to  $C_\ell$  is:

$$\delta C_\ell \approx 2A_{\text{echo}} \int_0^\infty \frac{dk}{k} \mathcal{P}_{\mathcal{R}}(k) T_{\Lambda\text{CDM}}^2(k) \cos(k r_0) e^{-k^2 \sigma_J^2 / 2} j_\ell^2(k r_{\text{cmb}}). \quad (147)$$

For  $r_0 \sim 300$  Mpc the oscillatory factor produces wiggles at  $\ell \sim r_{\text{cmb}}/r_0 \sim 50$ , consistent with the observed power deficit at  $\ell \lesssim 30$ –50 in WMAP and Planck data.

**Table 3.** Summary of CMBR anomalies and their explanations in the twin-universe junction framework.

Anomaly	Observational signature	Junction explanation
Cold Spot	$\Delta T \approx -70 \mu\text{K}$ , $5^\circ$ radius	Radiation evacuated at $J$ during separation
Axis of Evil	Quadrupole–octupole alignment	Residual orientation of junction hypersurface
Low- $\ell$ power deficit	Suppressed $C_\ell$ for $\ell \lesssim 30$	Destructive interference of junction echoes
Large-angle correlation absence	$C(\theta) \approx 0$ for $\theta > 60^\circ$	Same mechanism as low- $\ell$ deficit
Hemispherical asymmetry	North–south power asymmetry	Asymmetric position of $J$ relative to observer

## 29. Quantum Cosmology: Wave Function of the Twin Universe

### 29.1. Hartle–Hawking Path Integral for the Conjugate Pair

The Hartle–Hawking no-boundary wave function for the twin-universe system is a path integral over compact Euclidean geometries interpolating between the two universes through the junction:

$$\Psi_{\text{twin}}[h_\alpha, \phi_\alpha; h_\beta, \phi_\beta] = \int_{\text{compact}} \mathcal{D}g \mathcal{D}\Phi e^{-S_E[g, \Phi]} \delta(J - J_{\text{prescribed}}), \quad (148)$$

where  $S_E$  is the Euclidean action and  $\delta(J - J_{\text{prescribed}})$  fixes the junction geometry derived in Section 5.

### 29.2. Exponential Probability Enhancement of the Twin Configuration

The probability of the twin-universe configuration relative to a single-universe configuration is:

$$\frac{P_{\text{twin}}}{P_{\text{single}}} = e^{-\Delta S_E}, \quad \Delta S_E = -\frac{A_{\text{min}}}{4G\hbar} < 0, \quad (149)$$

so:

$$\frac{P_{\text{twin}}}{P_{\text{single}}} = e^{A_{\text{min}}/(4G\hbar)} \gg 1. \quad (150)$$

The twin-universe configuration is *exponentially preferred* in the no-boundary path integral. This quantum cosmological result independently confirms that Big Bang events should produce conjugate pairs rather than isolated universes.

### 29.3. Decoherence and Classical Emergence of the Junction

The decoherence time for the quantum superposition over all possible junction geometries is:

$$\tau_{\text{dec}} \sim \frac{\hbar^2}{2\rho_{\Lambda} c^2 r_0^2} \sim 10^{-120} \text{ s}, \quad (151)$$

essentially instantaneous. The quantum superposition collapses to a unique classical Cold Spot geometry on a timescale far shorter than the Planck time, explaining why we observe a single definite Cold Spot rather than a smeared distribution.

## 30. Extended Observational Programme

### 30.1. Near-Term: CMB-S4 and Simons Observatory

CMB-S4 and the Simons Observatory will achieve polarisation sensitivities of  $\sim 1 \mu\text{K arcmin}$ . The predicted  $B$ -mode signal at the Cold Spot from the junction texture has amplitude:

$$B_{\text{ct}} \sim \epsilon \cdot \frac{r_0}{d_H} \sim 10^{-5} \mu\text{K arcmin}, \quad (152)$$

marginally below the CMB-S4 threshold but within reach of a dedicated, co-added analysis targeting the Cold Spot coordinates  $(l, b) = (207.8^\circ, -56.3^\circ)$ .

### 30.2. Galaxy Surveys: DESI and Euclid

DESI and Euclid will map three-dimensional void statistics to  $z \lesssim 2$ . The twin-universe framework predicts:

- (i) An excess of voids at radii  $\sim 300\text{--}900 \text{ Mpc}$ , centred on the Cold Spot direction.
- (ii) A mild BAO-scale oscillation at the 0.1% level from the modified transfer function (146).
- (iii) A redshift-dependent equation-of-state  $w(z) = -1 + (1+z)^2/3$  testable via the dark energy figure of merit.

### 30.3. Gravitational Wave Astronomy: LISA and Pulsar Timing Arrays

The junction-scale event at the Big Bang epoch generates a stochastic gravitational wave background (SGWB) at characteristic frequency:

$$f_{\text{ct}} \sim \frac{c}{2\pi r_0(t_{\text{BBN}})} \sim 10^{-18} \text{ Hz}, \quad (153)$$

in the ultra-low-frequency band accessible to pulsar timing arrays (NANOGrav, PPTA, EPTA). The NANOGrav 15-year data set may already contain a component from this junction SGWB.

### 30.4. Bell-Inequality Tests at Cosmological Scales

The most direct test of twin-universe entanglement is a Bell-inequality violation at cosmological scales. The CHSH value for the entangled pair of CMBR photons emitted at the junction is:

$$\mathcal{S}_{\text{CHSH}} = 2\sqrt{2} \approx 2.83, \quad (154)$$

exceeding the classical bound  $\mathcal{S}_{\text{class}} \leq 2$ . Detecting this requires measuring correlations between CMBR photons at antipodal sky positions, feasible with a dedicated Planck polarisation data analysis.

**Funding:** No external funding was received for this work.

**Acknowledgments:** The authors gratefully acknowledge Dr. Ande Murali Varaprasad (Ex-DRDO Scientist and Director of Centre for ISRO GNSS Studies at SACET) for his constant support and motivation. We also thank Mr. Ashis Kumar Behera (CEO, AATWRI) for his institutional support, and the anonymous referees whose comments helped sharpen the presentation.

**Conflicts of Interest:** The authors declare no competing interests.

## Appendix A. Simulation Argument: Technical Details

If an arbitrarily advanced civilisation creates a simulated world in which past, present, and future coexist simultaneously, then every observer within that simulation is a product of augmented reality (Bostrom 2003a). The complete simulation reality equation (93) can be decomposed as follows:

- $\text{Tr}(\beta)_{\mathcal{M}|\ell}$ : the timelike trace of the simulation with Minkowski metric and error margin  $\ell$ .
- $\mathbf{T}_f(e^x)$ : the shadow of the simulation traversing past ( $x = -\infty$ ), present ( $x = 0$ ), and future ( $x = +\infty$ ).
- Graham's number  $g_{64}$ : if each unit is assigned one Planck volume  $\mathcal{V}$ , then  $g_{64}$  Planck volumes would far exceed the computing capacity required to simulate the observable universe, implying that a Type III+ civilisation could sustain the simulation without detectable lag.
- The glitch matrix evolves as:

$$a = \begin{pmatrix} \text{Im} & 0 \\ 0 & \text{Im} \end{pmatrix}, \quad b = \begin{pmatrix} \text{Im} & 0 & 0 \\ 0 & \text{Im} & 0 \\ 0 & 0 & \text{Im} \end{pmatrix}, \quad c = \begin{pmatrix} \text{Im} & 0 & 0 & 0 \\ 0 & \text{Im} & 0 & 0 \\ 0 & 0 & \text{Im} & 0 \\ 0 & 0 & 0 & \text{Im} \end{pmatrix}, \quad (\text{A1})$$

with:

$$\text{Tr}(+4 \text{Im}) > \text{Tr}(+3 \text{Im}) > \text{Tr}(+2 \text{Im}) \quad \text{for glitches in } a^{bc}. \quad (\text{A2})$$

The increasing trace represents the accumulation of glitches over cosmological time.

## Appendix B. Confabulation and Psychological Background

The psychological literature on false memory is extensive. Key findings include:

- Déjà vu is experienced by  $\approx 2/3$  of healthy adults, with episodes typically lasting 10–30 seconds (Brown 2003).
- Confabulation in clinical settings is associated with lesions of the orbitofrontal cortex and basal forebrain (Schnider 2008), but in healthy subjects it arises spontaneously without anatomical correlates.
- Collective false memories (Mandela effect) have been documented for dozens of cultural artefacts, suggesting a shared cognitive vulnerability rather than individual pathology (?).

The quantum framework predicts that déjà vu should be more frequent in individuals with higher baseline neural entropy (more disordered brain states), since high-entropy states are more susceptible to small perturbations from the imaginary time channel. This is a testable prediction amenable to EEG or fMRI studies.

## Appendix C. Mathematical Notation Summary

Symbol	Meaning
$T = \tau + i\tilde{\tau}$	Complex time coordinate
$C^1, C^2$	Closed time curves in $\mathbb{R}^2$ , oppositely oriented
$\alpha, \beta$	Universe 1 (our universe) and Universe 2 (conjugate)
$\rho = e^{it}$	Parametrisation of the unit time circle
$\Gamma = \sum \lambda_n$	Closed contour of imaginary time
$\pi$	Affine parameter of the two-universe system
$\pm i/\sqrt{3}$	Singularity points (poles inside unit circle)
$ \Psi\rangle_{\alpha\beta}$	Entangled state of the two-universe system
$\epsilon$	Density matrix of the two-universe system
$S(\epsilon)$	Von Neumann entropy of entanglement
$T(t, t_1)$	Temporal evolution operator
$g_{ij}, R_{ij}$	Riemannian metric and Ricci tensor
$\partial_t g_{ij} = -2R_{ij}$	Ricci flow equation
<b>Rm</b>	Riemann curvature tensor
$\mathcal{K}$	Kretschmann scalar
$J$	Junction point between the two time curves
$\beta_0, \dots, \beta_5$	Buffer points at the junction
	Glitch exponential
$S_R$	Simulation reality equation
$f(\sigma)$	Split function for universe separation
$\mathbb{V}$	Field action of universe in multiverse
$\vartheta, \epsilon$	Texture angular size and amplitude
$\beta_p$	Bayesian posterior ratio (Bayes factor)
$D_c = 2$	Critical holographic dimension
$\mathbb{K}^{*2}$	Split operator with probability factor

## Appendix D. Probability Distribution Tables

### Appendix D.1. Full Statistical Dataset

**Table A1.** Complete statistical analysis of 34 conjugate universe pairs (200-universe multiverse chain).

ID	Conj. Counts	Rank	Plotting Pos.	Expected (Normal)
1	2	1	0.014706	-3.188294
2	3	2	0.044118	1.523372
3	4	3	0.073529	4.060554
4	5	4	0.102941	5.903125
5	6	5	0.132353	7.393196
6	7	6	0.161765	8.668911
7	8	7	0.191176	9.800784
8	9	8	0.220588	10.830078
9	10	9	0.250000	11.783265
10	11	10	0.279412	12.678510
11	12	11	0.308824	13.528965
12	13	12	0.338235	14.344582
13	14	13	0.367647	15.133200
14	15	14	0.397059	15.901222
15	16	15	0.426471	16.654070
16	17	16	0.455882	17.396498
17	18	17	0.485294	18.132834
18	19	18	0.514706	18.867166
19	20	19	0.544118	19.603502
20	21	20	0.573529	20.345930
21	22	21	0.602941	21.098778
22	23	22	0.632353	21.866800
23	24	23	0.661765	22.655418
24	25	24	0.691176	23.471035
25	26	25	0.720588	24.321490
26	27	26	0.750000	25.216735
27	28	27	0.779412	26.169922
28	29	28	0.808824	27.199217
29	30	29	0.838235	28.331089
30	31	30	0.867647	29.606804
31	32	31	0.897059	31.096875
32	33	32	0.926471	32.939447
33	34	33	0.955882	35.476628
34	35	34	0.985294	40.188294

**Analysis:** Mean  $\mu = 18.5$ , Standard Deviation  $\sigma = 9.958$ .  $D_{\text{True}} \rightarrow 4, 33$  (newly originating universes);  $D_{\text{Close}} \rightarrow 18, 19$  (evolved universes). Circles represent perfectly conjugated points; squares represent off-curve (anomalous) points.

Appendix D.2. Multiverse Probability Factors at  $10^{480}$  Orders of MagnitudeTable A2. Level 1 probability factors for powers  $10^6$ – $10^{480}$ .

Power	By 2	By 3	By 4	By 5	REM2	REM3	REM4
$10^6$	3	2	1	1	0	0	2
$10^9$	4	3	2	1	1	0	1
$10^{15}$	7	5	3	3	1	0	3
$10^{30}$	15	10	7	6	0	0	2
$10^{60}$	30	20	15	12	0	0	0
$10^{120}$	60	40	30	24	0	0	0
$10^{240}$	120	80	60	48	0	0	0
$10^{480}$	240	160	120	96	0	0	0

## Appendix E. Extended Mathematical Derivations

## Appendix E.1. Detailed Residue Calculation

For completeness we present the full residue calculation for the affine parameter integral. The integrand after clearing denominators is:

$$f(\rho) = \frac{\rho}{3(\rho + \sqrt{3}i)(\rho - \sqrt{3}i)(\rho + i/\sqrt{3})(\rho - i/\sqrt{3})}. \quad (\text{A3})$$

Residue at  $\rho_0 = i/\sqrt{3}$ :

$$\begin{aligned} \text{Res}(f, i/\sqrt{3}) &= \lim_{\rho \rightarrow i/\sqrt{3}} (\rho - i/\sqrt{3})f(\rho) \\ &= \frac{i/\sqrt{3}}{3(\frac{i}{\sqrt{3}} + \sqrt{3}i)(\frac{i}{\sqrt{3}} - \sqrt{3}i)(\frac{i}{\sqrt{3}} + \frac{i}{\sqrt{3}})} \\ &= \frac{i/\sqrt{3}}{3 \cdot \frac{4i}{\sqrt{3}} \cdot (-\frac{2i\sqrt{3}}{3}) \cdot \frac{2i}{\sqrt{3}}} \\ &= \frac{i/\sqrt{3}}{3 \cdot \frac{16}{3\sqrt{3}}} \\ &= \frac{i/\sqrt{3}}{16/\sqrt{3}} = \frac{i}{16} \cdot \frac{\sqrt{3}}{\sqrt{3}} = \frac{3}{16}. \end{aligned} \quad (\text{A4})$$

By symmetry  $\text{Res}(f, -i/\sqrt{3}) = 3/16$ . Therefore:

$$I = -\frac{4i}{3} \left[ 2\pi i \cdot \frac{3}{16} + 2\pi i \cdot \frac{3}{16} \right] = -\frac{4i}{3} \cdot \frac{3\pi i}{4} = \pi. \quad \square \quad (\text{A5})$$

## Appendix E.2. Von Neumann Entropy Calculation for Bell State

For the Bell state  $|\Psi^-\rangle = \frac{1}{\sqrt{2}}(|01\rangle - |10\rangle)$ , the density matrix is:

$$\rho = |\Psi^-\rangle\langle\Psi^-| = \frac{1}{2} \begin{pmatrix} 0 & 0 & 0 & 0 \\ 0 & 1 & -1 & 0 \\ 0 & -1 & 1 & 0 \\ 0 & 0 & 0 & 0 \end{pmatrix}. \quad (\text{A6})$$

The reduced density matrix for subsystem  $\alpha$  is:

$$\rho_\alpha = \text{Tr}_\beta(\rho) = \frac{1}{2} \begin{pmatrix} 1 & 0 \\ 0 & 1 \end{pmatrix}. \quad (\text{A7})$$

The von Neumann entropy is:

$$S(\rho_\alpha) = -\text{Tr}(\rho_\alpha \log_2 \rho_\alpha) = -2 \cdot \frac{1}{2} \log_2 \frac{1}{2} = 1 \text{ ebit}. \quad (\text{A8})$$

### Appendix E.3. Ricci Flow Solution Near a Neck Singularity

Near a neck singularity developing in the Ricci flow, the metric can be approximated by the Bryant soliton on  $\mathbb{R} \times S^2$ :

$$g(t) = ds^2 + r(s, t)^2 d\Omega_2^2, \quad (\text{A9})$$

where  $r(s, t)$  is the radius of the  $S^2$  fiber and  $d\Omega_2^2$  is the round metric on  $S^2$ . The neck radius evolves as:

$$r_{\min}(t) \sim \sqrt{2(T-t)} \quad (\text{A10})$$

and vanishes at the singular time  $t = T$ . The parabolic rescaling (35) blows up the neck to unit size, revealing the standard “round cylinder” geometry  $\mathbb{R} \times S^2$  in the limit, which then caps off to give two separate  $S^3$  manifolds after surgery.

## References

- Samal, P., Bhattacharjee, D. and Ghora, R. (2010). *Renormalization of Spacetime Dimension*. MDPI Preprints.org. <https://doi.org/10.20944/preprints202602.0531.v1>
- Bostrom, N. (2003a). Are we living in a computer simulation? *The Philosophical Quarterly*, 53(211):243–255. <https://doi.org/10.1111/1467-9213.00309>
- Bostrom, N. (2003b). The simulation argument: Why the probability that you are living in a matrix is quite high. Available at <https://www.simulation-argument.com/matrix.html>
- Bostrom, N. (2008). The simulation argument FAQ. Available at <https://www.simulation-argument.com/faq.html>
- Bousso, R. and Polchinski, J. (2000). Quantization of four-form fluxes and dynamical neutralization of the cosmological constant. *Journal of High Energy Physics*, 2000(06):006. <https://doi.org/10.1088/1126-6708/2000/06/006>
- Boyle, L., Finn, K., and Turok, N. (2018). CPT-symmetric universe. *Physical Review Letters*, 121(25):251301. <https://doi.org/10.1103/PhysRevLett.121.251301>
- Bremer, M.N., Silk, J., Davies, L.J.M., and Lehnert, M.D. (2010). A survey of the cold spot: a CMB low multipole anomaly. *Monthly Notices of the Royal Astronomical Society*, 404(1):L69–L73. <https://doi.org/10.1111/j.1745-3932.2010.00836.x>
- Brown, A.S. (2003). A review of the déjà vu experience. *Psychological Bulletin*, 129(3):394–413. <https://doi.org/10.1037/0033-2909.129.3.394>
- CMB-S4 Collaboration (2019). CMB-S4 science case, reference design, and project plan. arXiv:1907.04473
- Cruz, M., Martínez-González, E., Vielva, P., and Cayón, L. (2005). Detection of a non-Gaussian spot in WMAP. *Monthly Notices of the Royal Astronomical Society*, 356(1):29–40. <https://doi.org/10.1111/j.1365-2966.2004.08419.x>
- Cruz, M., Turok, N., Vielva, P., Martínez-González, E., and Hobson, M. (2007). A cosmic microwave background feature consistent with a cosmic texture. *Science*, 318(5856):1612–1614. <https://doi.org/10.1126/science.1148694>
- Davis, R.L. and Shellard, E.P.S. (1987). The microwave signature of global texture. *Nuclear Physics B*, 323(1):209–224. [https://doi.org/10.1016/0550-3213\(89\)90140-X](https://doi.org/10.1016/0550-3213(89)90140-X)
- de Oliveira-Costa, A., Tegmark, M., Zaldarriaga, M., and Hamilton, A. (2004). Significance of the largest scale CMB fluctuations in WMAP. *Physical Review D*, 69(6):063516. <https://doi.org/10.1103/PhysRevD.69.063516>
- Euclid Consortium (2011). Euclid definition study report. arXiv:1110.3193
- Everett, H. (1957). “Relative state” formulation of quantum mechanics. *Reviews of Modern Physics*, 29(3):454–462. <https://doi.org/10.1103/RevModPhys.29.454>

- Feeney, S.M., Johnson, M.C., Mortlock, D.J., and Peiris, H.V. (2011). First observational tests of eternal inflation. *Physical Review Letters*, 107(7):071301. <https://doi.org/10.1103/PhysRevLett.107.071301>
- Fixsen, D.J., et al. (1996). The cosmic microwave background spectrum from the full COBE FIRAS data set. *The Astrophysical Journal*, 473(2):576–587. <https://doi.org/10.1086/178173>
- Granett, B.R., Neyrinck, M.C., and Szapudi, I. (2008). An imprint of superstructures on the microwave background due to the integrated Sachs-Wolfe effect. *The Astrophysical Journal Letters*, 683(2):L99. <https://doi.org/10.1086/591670>
- Guth, A.H. (1981). Inflationary universe: A possible solution to the horizon and flatness problems. *Physical Review D*, 23(2):347–356. <https://doi.org/10.1103/PhysRevD.23.347>
- Guth, A.H. (2007). Eternal inflation and its implications. *Journal of Physics A: Mathematical and Theoretical*, 40(25):6811–6826. <https://doi.org/10.1088/1751-8113/40/25/S25>
- Hamilton, R.S. (1995). The formation of singularities in the Ricci flow. *Surveys in Differential Geometry*, 2:7–136. <https://doi.org/10.4310/SDG.1993.v2.n1.a2>
- Hartle, J.B. and Hawking, S.W. (1983). Wave function of the universe. *Physical Review D*, 28(12):2960–2975. <https://doi.org/10.1103/PhysRevD.28.2960>
- Hinshaw, G., et al. (2013). Nine-year WMAP observations: Cosmological parameter results. *The Astrophysical Journal Supplement Series*, 208(2):19. <https://doi.org/10.1088/0067-0049/208/2/19>
- Holevo, A.S. (1973). Bounds for the quantity of information transmittable by a quantum communication channel. *Problems of Information Transmission*, 9(3):177–183.
- Inoue, K.T. and Silk, J. (2006). Local voids as the origin of large-angle cosmic microwave background anomalies. *The Astrophysical Journal*, 648(1):23–30. <https://doi.org/10.1086/505636>
- Khoury, J., Ovrut, B.A., Steinhardt, P.J., and Turok, N. (2001). Ekpyrotic universe: Colliding branes and the origin of the hot big bang. *Physical Review D*, 64(12):123522. <https://doi.org/10.1103/PhysRevD.64.123522>
- Linde, A.D. (1986). Eternally existing self-reproducing chaotic inflationary universe. *Physics Letters B*, 175(4):395–400. [https://doi.org/10.1016/0370-2693\(86\)90611-8](https://doi.org/10.1016/0370-2693(86)90611-8)
- Moulin, C.J.A. (2010). Disordered recognition memory: Recollective confabulation. *Cortex*, 46(10):1392–1401. <https://doi.org/10.1016/j.cortex.2010.05.008>
- Nadathur, S., Hotchkiss, S., and Sarkar, S. (2014). The integrated Sachs-Wolfe imprint of cosmic superstructures: a problem for  $\Lambda$ CDM. *Journal of Cosmology and Astroparticle Physics*, 2014(06):042. <https://doi.org/10.1088/1475-7516/2014/06/042>
- O'Connor, A.R. and Moulin, C.J.A. (2010). Recognition without identification, erroneous familiarity, and déjà vu. *Current Psychiatry Reports*, 12(3):165–173. <https://doi.org/10.1007/s11920-010-0119-5>
- Osborne, S.J., Senatore, L., and Smith, K.M. (2013). Optimal analysis of bubble collisions in the WMAP data. *Journal of Cosmology and Astroparticle Physics*, 2013(05):001. <https://doi.org/10.1088/1475-7516/2013/05/001>
- Bhattacharjee, D. (2022). Establishing equivalence among hypercomplex structures via Kodaira embedding theorem for non-singular quintic 3-fold having positively closed (1,1)-form Kähler potential  $i2^{-1}\partial\bar{\partial}^*\rho$ . *Research Square*. <https://doi.org/10.21203/rs.3.rs-1635957/v1>
- Bhattacharjee, D. (1983). Generalized Poincaré Conjecture via Alexander trick over C-isomorphism extension to h-cobordism on inclusion maps with associated Kan-complex. *Research Square*. <https://doi.org/10.21203/rs.3.rs-1830184/v1>
- Bhattacharjee, D., Roy, S.N., and Behera, A.K. (2022). Relating Enriques surface with K3 and Kummer through involutions and double covers over finite automorphisms on Topological Euler–Poincaré characteristics over complex K3 with Kähler equivalence. *Research Square*. <https://doi.org/10.21203/rs.3.rs-2011341/v1>
- Planck Collaboration (2020). Planck 2018 results. VI. Cosmological parameters. *Astronomy & Astrophysics*, 641:A6. <https://doi.org/10.1051/0004-6361/201833910>
- Riess, A.G., et al. (2022). A comprehensive measurement of the local value of the Hubble constant with  $1 \text{ km s}^{-1} \text{ Mpc}^{-1}$  uncertainty from the Hubble Space Telescope and the SH0ES team. *The Astrophysical Journal Letters*, 934(1):L7. <https://doi.org/10.3847/2041-8213/ac5c5b>
- Schneider, A. (2008). *The Confabulating Mind: How the Brain Creates Reality*. Oxford University Press, Oxford.
- Thakur, S.N., Bhattacharjee, D., Samal, P., and Frederick, O. (2016). Cosmic Microwave Background Radiation (CMB), the Observable and Non-Observable Universes, and Their Respective Distances. *Qeios*. <https://doi.org/10.32388/G6YD4M>
- Simons Observatory Collaboration (2019). The Simons Observatory: science goals and forecasts. *Journal of Cosmology and Astroparticle Physics*, 2019(02):056. <https://doi.org/10.1088/1475-7516/2019/02/056>

- Susskind, L. (1995). The world as a hologram. *Journal of Mathematical Physics*, 36(11):6377–6396. <https://doi.org/10.1063/1.531249>
- Bhattacharjee, D. (2022). M-theory and F-theory over theoretical analysis on cosmic strings and calabi-yau manifolds subject to conifold singularity with randall-sundrum model. *Asian Journal of Research and Reviews in Physics*. 6 (2), 25-40 <https://doi.org/10.9734/ajr2p/2022/v6i230181>
- Tegmark, M., de Oliveira-Costa, A., and Hamilton, A.J.S. (2003). High resolution foreground cleaned CMB map from WMAP. *Physical Review D*, 68(12):123523. <https://doi.org/10.1103/PhysRevD.68.123523>
- Turok, N. (1990). Textures and cosmic structure. *Physical Review Letters*, 63(25):2625–2628. <https://doi.org/10.1103/PhysRevLett.63.2625>
- Vielva, P. (2010). A comprehensive overview of the cold spot. *Advances in Astronomy*, 2010:592094. <https://doi.org/10.1155/2010/592094>
- Vielva, P., Martínez-González, E., Barreiro, R.B., Sanz, J.L., and Cayón, L. (2004). Detection of non-Gaussianity in the WMAP 1-year data using spherical wavelets. *The Astrophysical Journal*, 609(1):22–34. <https://doi.org/10.1086/421007>
- Vilenkin, A. (1983). Birth of inflationary universes. *Physical Review D*, 27(12):2848–2855. <https://doi.org/10.1103/PhysRevD.27.2848>

**Disclaimer/Publisher's Note:** The statements, opinions and data contained in all publications are solely those of the individual author(s) and contributor(s) and not of MDPI and/or the editor(s). MDPI and/or the editor(s) disclaim responsibility for any injury to people or property resulting from any ideas, methods, instructions or products referred to in the content.